

Modeling the Mars Atmosphere for Monte Carlo Simulations
of the Mars 2001 Odyssey Aerobraking Mission

by
Alicia Marie Dwyer
B.S. in Physics, May 1999, Creighton University

A Thesis submitted to the Faculty of the
School of Engineering and Applied Science

of

George Washington University
in partial fulfillment of the requirements for the degree of
Master of Science

August 31, 2001

Thesis directed by
Robert H. Tolson
Professor of Engineering and Applied Science

This research was conducted at NASA Langley Research Center

Abstract

The method of aerobraking has proved successful in missions to both Mars and Venus. Aerobraking uses the atmosphere of the planet rather than chemical propulsion to reduce the size of the orbit of a spacecraft. In October 2001, aerobraking will again be used by the Mars 2001 Odyssey orbiter to obtain a desired science mapping orbit. The success of the aerobraking mission depends on how accurately the behavior of the atmosphere is known. Knowledge of the Mars atmosphere is obtained from previous passes through the atmosphere by landers such as Viking and Pathfinder, and aerobraking passes recorded by orbiters like Mars Global Surveyor. The previous mission data, combined with an understanding of the fundamental physics of the atmosphere, become the basis of atmospheric models. The models, used in the design and operation of spacecraft, are critical to mission success.

This paper briefly summarizes the structure and driving forces that affect the atmosphere of Mars. Current models of the atmosphere used for aerobraking missions are reviewed and compared to the most recent atmospheric data from the planet. Finally, a discussion of a statistical model of the Mars atmosphere, developed specifically for Monte Carlo simulations of aerobraking operations for the Mars 2001 mission, is provided.

Acknowledgements

The author would like to express gratitude to Dr. Robert H. Tolson for his guidance, assistance, encouragement and patience over the past two years. She would also like to thank Richard Powell for the opportunity to work with the outstanding planetary team of the Mars 2001 Odyssey Mission. Thank you is also extended to Michelle M. Munk, Paul V. Tartabini and John T. Aguirre of the Vehicle Analysis Branch at NASA Langley Research Center for their assistance in many areas including Mars-GRAM, UNIX systems and model validation. A sincere thanks to Paul E. Escalera, Michelle M. Munk, and Dr. Robert H. Tolson for the many hours spent editing papers.

The author would like to express her appreciation to the faculty and staff of the George Washington University's Joint Institute for Advancement of Flight Sciences for the challenges and rewarding experiences of the past two years. Finally, the author would like to thank her family and Matt J. Cianciolo for their continued support throughout her formal education. The author could not have made it this far without the help of many people. Thank you.

Table of Contents

Abstract.....	ii
Acknowledgements.....	iii
Table of Contents.....	iv
List of Figures.....	vi
Nomenclature.....	viii
List of Tables.....	x
Chapter 1. Introduction.....	1
1.1 Characteristics of the Mars Atmosphere.....	3
1.2 Structure of the Atmosphere.....	6
1.3 Mars Atmosphere as Experienced by Mars Global Surveyor.....	8
Chapter 2. Current Models of the Mars Atmosphere.....	14
2.1 Mars-GRAM 3.7.....	15
2.2 Mars-GRAM 2000.....	16
Chapter 3. Comparison of Mars-GRAM to MGS Data.....	18
3.1 Comparison of Mars-GRAM 3.7 with MGS Density Data.....	18
3.2 Comparison of Mars-GRAM 2000 with MGS Density Data.....	20
3.3 Comparison of Scale Heights.....	23
3.4 Lessons for the Mars 2001 Mission.....	25
3.5 Improving Comparisons With Mars-GRAM 2000.....	26
Chapter 4. Monte Carlo Modeling Methods.....	32
4.1 Monte Carlo Simulation Overview.....	34
4.2 Planetary Wave Models.....	34

4.2.1	Mars-GRAM Wave Model	35
4.2.2	Reference Monte Carlo Wave Model	37
4.3	Monte Carlo Model.....	41
4.4	Model Validation	44
4.4.1	Persistence Test.....	44
4.4.2	Reconstruction of Wave Amplitude and Phase	47
4.4.3	Wave Model Prediction	50
4.5	Operational Prediction Schemes.....	52
4.6	Monte Carlo Model Summary	53
Chapter 5. Summary		56
References.....		58
Appendix A. Aerobraking in a Constant Density Scale Height Atmosphere		A-1
Appendix B. Namelists for MG3.7 and MG2K.....		B-1
Appendix C. Equipotential Surfaces and the Relationship to Reference Ellipsoid.....		C-1
Appendix D. MGS Waves 1 Through 5.....		D-1
Appendix E. Plots of the Reference “Low Wave” Model		E-1

List of Figures

Figure 1. Graphical representation of aerobraking.	1
Figure 2. Solar longitude definition.	5
Figure 3. Scale height definition.	9
Figure 4. Properties of the MGS and M-01 aerobraking orbits at periapsis.	11
Figure 5. Phase 1 inbound and outbound log densities at 140 km versus time.	12
Figure 6. Ratio of MGS data to MG 3.7 predicted data for the nominal dust case.	19
Figure 7. Ratio of MGS data to MG 3.7 predicted data (complete range).	19
Figure 8. Density at 130 km versus latitude for MGS data including Phase 1 and 2.	20
Figure 9. Ratio of MGS to MG2K data for the nominal dust case.	21
Figure 10. Ratio of MGS to MG2K data for the dust storm case.	22
Figure 11. Scale height calculations of MGS data from MG3.7 and MG2K.	23
Figure 12. Scale height calculations using MGS data at lower altitudes.	24
Figure 13. Modified ratios of MGS to MG2K with nominal settings.	28
Figure 14. Modified ratios of MGS to MG2K with dust storm settings.	29
Figure 15. Seven point running mean of the wave model and offset; sigma for each mean.	30
Figure 16. Ratio of MGS to MG2K densities at periapsis versus latitude, nominal settings.	31
Figure 17. Wave 1 amplitude and phase.	39
Figure 18. Wave 2 amplitude and phase.	40
Figure 19. Wave 3 amplitude and phase.	41
Figure 20. Standard deviation of the residuals for wave model solution.	42
Figure 21. Histograms for points 1, 8, 22, and 30 from sliding wave model solutions.	43
Figure 22. Persistence results using MGS periapsis density and scale height.	45
Figure 23. Persistence for one realization of MC model densities.	47

Figure 24. Wave 1 amplitude and phase recovered from one realization of the MC model.	48
Figure 25. Wave 2 amplitude and phase recovered from one realization of the MC model.	49
Figure 26. Wave 3 amplitude and phase recovered from one realization of the MC model.	49
Figure 27. Prediction capability for the 30-orbit wave model solution; MGS Phase 2 data.	51
Figure 28. Prediction capability for the 30 orbit wave model solution: MC Phase 2 data.	51
Figure 29. One realization of MC model for MGS: $\rho_0=1$ (ρ) and 5 orbit running mean (ρ_5). ..	53
Figure 30. Heat rate versus apoapsis for one Mars 2001 mission simulation.....	54

Nomenclature

A	Spacecraft cross-sectional area
A_n	Wave amplitude in MC wave model for wave number n
A_o	Density multiplier
a_z	Acceleration in the z direction
B_o	Mean perturbation density offset in Mars-GRAM 2000 wave model
$B_{1,2,3}$	Wave amplitudes in Mars-GRAM 2000 wave model
CF	Climate factors
C_z	Force coefficient in the z direction
EUV	Extreme ultra violet
GCM	General Circulation Model
h	Height above reference ellipsoid
h_{off}	Altitude offset
H_s	Scale height
LDW	Longitude-dependent wave
L_s	Longitude of the Sun
LST	Local Solar Time
m	Spacecraft mass
M-01	Mars 2001 Odyssey
Mars-GRAM	Mars Global Reference Atmospheric Model
MC	Monte Carlo
MG2K	Mars-GRAM version 2000
MG3.7	Mars-GRAM version 3.7

MGCM	Mars General Circulation Model
MGS	Mars Global Surveyor
MLE	Maximum likelihood estimator
MTGCM	Mars Thermospheric General Circulation Model
n	Wave number
NASA	National Aeronautical and Space Administration
NCAR	National Center for Atmospheric Research
PDF	Probability distribution function
V	Velocity of the spacecraft relative to the atmosphere
$\Phi_{1,2,3}$	Wave phases in Mars-GRAM 2000 wave model
ϕ	Latitude
λ	Longitude
λ_n	Phase in MC wave model for wave number n
ρ	Density
ρ_o	Density calculated by Mars-GRAM
ρ_r	Reference density

List of Tables

Table 1. Input Values to Account for the Dust Storm in Mars-GRAM 2000.....	22
Table 2. Summary of 10 Realizations of the Monte Carlo Model.....	47

Chapter 1. Introduction

Aeroassist maneuvers may be performed on a spacecraft in a planetary atmosphere to change the trajectory of the spacecraft. Central to any aeroassist maneuver is the use of the atmospheric forces of lift and drag to perform a preplanned behavior of the spacecraft. Aeroassist maneuvers include aerobraking, aeroentry, aerocapture, precision landing and hazard detection and avoidance [1]. Specifically, the use of aerobraking is being explored and applied to future missions to Mars.

Aerobraking utilizes the upper atmosphere of a planet to gradually reduce the velocity of an orbiting spacecraft reducing the eccentricity and semi-major axis to obtain a desired orbit around the planet. A graphical representation of aerobraking is provided in Figure 1.

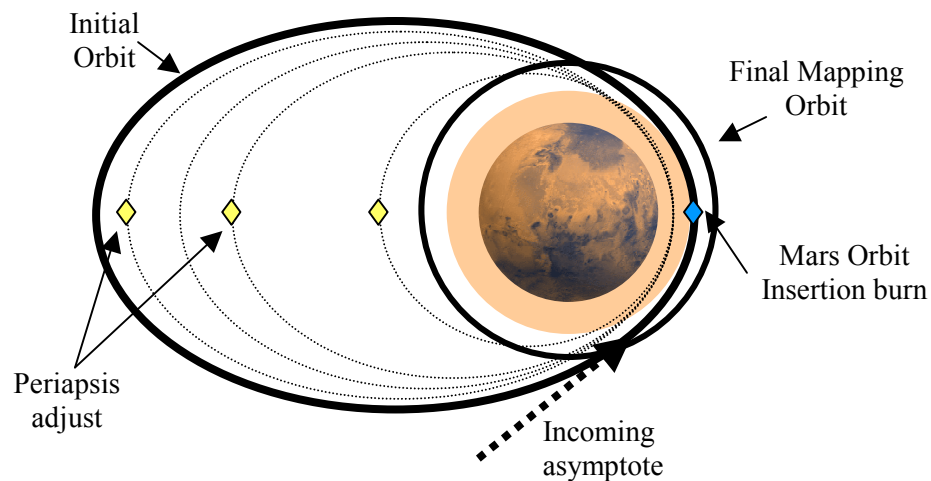


Figure 1. Graphical representation of aerobraking.

The trajectory of a spacecraft, aligned with the *incoming asymptote*, will be affected by the gravity and atmosphere of the planet. The *Mars orbital insertion* burn provides the change in velocity required to place the spacecraft in orbit around the planet. Successive *periapsis adjustment* burns are made at the apoapsis of selected orbits to change the height of periapsis. Reduction of the periapsis altitude increases the amount of drag on the spacecraft, which

reduces the velocity and eccentricity of the orbit and lowers apoapsis altitude. This process is repeated until the spacecraft is in a desired orbit about the planet. Aerobraking has proven successful, first at Venus, with the Magellan spacecraft in the summer of 1993 [2], then at Mars in 1997-1999 with the Global Surveyor [3].

The advantage of using aerobraking at Mars is in the significant reduction of propellant mass. The ratio of liftoff to payload mass is reduced resulting in a lower overall cost of the mission and allows for larger science payloads. One example of the savings offered by aerobraking is seen by comparing Mars Global Surveyor (MGS) to the Mars Observer mission. The mapping orbits for the two were the same: low sun-synchronous, near circular, and near polar. Mars Observer was launched in 1992 and failed three days before entering the Mars orbit in August 1993 [4]. Mars Observer carried two more instruments than MGS and a chemical propellant system to obtain the desired orbit. The payload difference between MGS and the Mars Observer was only 81 kg, but the overall launch mass of MGS was 2.4 times smaller (1060 kg versus 2572 kg). The chemical propulsive velocity required to move from the capture orbit to the near circular mapping orbit using aerobraking was 11 times lower for MGS (125 m/s versus 1367 m/s) [4]. The majority of the mass difference was due to the large amounts of fuel and oxidizer required to circularize the orbit for Mars Observer. Therefore, aerobraking allowed for a lighter, smaller, less expensive (by a factor of 5) launch vehicle, for a total of \$200 million savings. This substantial amount makes interplanetary travel and exploration affordable, and aerobraking appealing for use in future missions.

However, aerobraking is not a risk free endeavor. It involves balancing and optimizing the tradeoffs between aerodynamics, thermal loads, guidance, and navigation and control [5]. Critical to the mission is the characterization of the entry environment (i.e., the upper atmosphere) to predict the aerodynamic forces to ensure that the vehicle is properly designed

for the thermal and propulsive requirements. Effective use of aerobraking requires detailed knowledge of the Martian atmosphere. Therefore, the physical processes controlling the environment, climate, atmospheric motions and transport of aerosols (i.e., dust) must be understood [6].

The year 2001 offers another opportunity for aerobraking at Mars with the launch of the Mars 2001 Odyssey (M-01) orbiter, which is scheduled to reach the planet in October. This paper will review important characteristics of the atmosphere of Mars revealed by past missions and discuss how the characteristics are used to develop models of the atmosphere of Mars. Two versions of the widely used Mars Global Reference Atmospheric Model (Mars-GRAM) are reviewed and compared to the most recent atmospheric data obtained by MGS. Finally, a statistical model of the atmosphere of Mars, which incorporates the knowledge of the atmospheric characteristics and Mars-GRAM, is proposed for the Monte Carlo simulations of the M-01 aerobraking mission.

1.1 Characteristics of the Mars Atmosphere

Until 1997, there were only three in-situ vertical structures recorded of the Mars atmosphere. They were obtained from the Viking Landers 1 and 2 (1976) and Mars Pathfinder (1997). Between 1997-1999 the aerobraking mission of MGS provided approximately 1600 more vertical structures of the upper atmosphere of Mars between the altitudes of 110 km and 170 km. Studies of the Martian atmosphere by orbiters and landers suggest that the atmospheric density is affected by the physical characteristics of the planet as well as the season, latitude, altitude, atmospheric dust level, distance from the sun and local solar time (LST). The impact of each of these parameters on the atmosphere of Mars must be considered when developing models of the Martian atmosphere.

Information obtained from past missions indicates that the physical characteristics of the planet affect the atmosphere. The atmospheric density, pressure and temperature are directly affected by the size of the planet, the gravity force, the planetary distance from the sun and the amount of material in the atmosphere. Mars has one-tenth the mass and one-half of the radius of the Earth which result in a surface gravity approximately one-third of the Earth's. The gravity field and atmospheric mass result in an average surface density of approximately 0.02 kg/m^3 compared to the Earth's 1.217 kg/m^3 and a surface pressure approximately 7×10^{-6} bar, compared to 1.013 bars (1 atm) at sea level on Earth ($1 \text{ bar} = 100,000 \text{ N/m}^2$).

With its sparse atmosphere and distance from the Sun, the mean surface temperature of Mars is approximately 217 K, lower than the 288 K on Earth. As a result of the low atmospheric density of Mars, relative to the Earth, a large temperature gradient is found between the equator and the pole: 40% difference from the mean temperature compared to a 15% difference from the mean found on Earth [7]. The latitudinal temperature gradient is a likely cause of the high wind speeds (up to 30 m/s near the surface [8]) observed on the planet.

Planetary winds are also driven by the topography of the planet [8]. The southern hemisphere is littered with impact craters and rough terrain, compared to the plains of the high northern hemisphere. The terrain of the southern hemisphere induces turbulent flow over the surface, which initiates dust storms in the region. Mars also has very distinct topographical features like Olympus Mons, the largest known volcano in the solar system extending 29 km high, and the Valles Marineris, a canyon 5000 km long and 6 km deep. These landforms strongly effect the general circulation of the atmosphere in the surrounding regions. In addition to the physical characteristics of Mars, seasonal, diurnal, and latitudinal variations affect the atmosphere of Mars. The effects of each are described in detail.

Due to the obliquity of the planet, Mars experiences seasons similar to the Earth's. Latitudinal and seasonal variations are due to changes in the solar heat input which depend on changes in the latitude of the Sun and the planet-Sun distance (particularly important for Mars due to its large orbital eccentricity of 0.09 compared to the Earth's 0.01). On Mars the seasons are denoted by solar longitude (L_s). For example, Figure 2 shows $L_s=0^\circ$ which corresponds to the vernal equinox (i.e., the Sun moves into the northern hemisphere), $L_s=90^\circ$ marks the summer solstice, $L_s=180^\circ$ is the autumnal equinox and $L_s=270^\circ$ corresponds to the winter solstice. The perihelion of Mars occurs at $L_s=250^\circ$, just before the winter solstice.

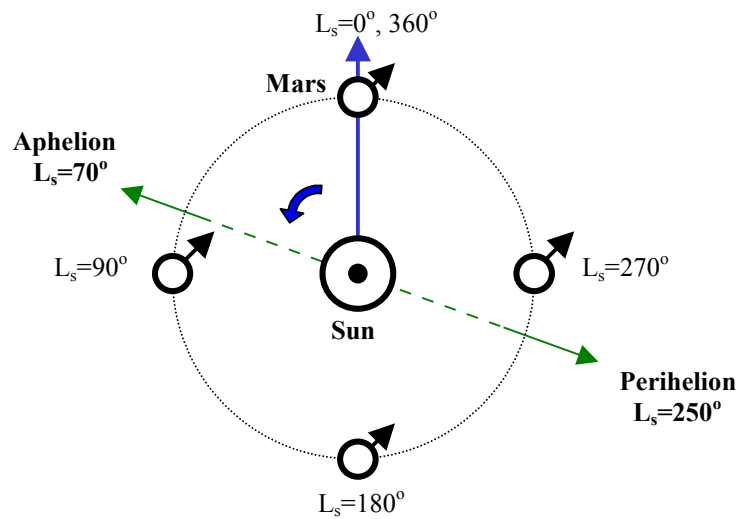


Figure 2. Solar longitude definition.

Dust storms have a strong seasonal effect in the atmosphere. Since the majority of the planet is covered with dust, the circulation of the atmosphere stirs the dust from the surface. This occurs in both localized storms extending approximately 250 km wide and up to 7 km high in the atmosphere to global storms which cover most of one or both hemispheres of Mars [8]. Global dust storms begin primarily in the southern hemisphere summer ($L_s=180^\circ$ to 320°). The amount of dust in the atmosphere is measured by a non-dimensional dust opacity. Dust opacity can range from zero on a clear day to three during a dust storm. The increased number

of particles in the atmosphere near the surface absorbs more solar radiation resulting in an increase in atmospheric temperature. The dust heating near the surface causes expansion of the entire atmosphere [6] which results in higher densities in the upper atmospheres. Therefore, there is a strong coupling between the upper and lower atmospheres of Mars.

The temperature of the atmosphere is also affected by the local solar time (*LST*) (i.e., time of day). Diurnal variations in solar heating result as the planet rotates every 24 hours and 37 minutes (1 sol). A large change in temperature from day to night is experienced, resulting in diurnal atmospheric (density) tides.

The combined effects on the density of the atmosphere from the seasonal, diurnal, latitudinal, topographic variations and dust storms produce upward-propagating atmospheric waves and tides [9]. These atmospheric phenomena were observed during the MGS aerobraking mission [10]. Models of the Mars atmosphere attempt to capture these effects.

1.2 Structure of the Atmosphere

The physical and orbital characteristics of the planet have established three identifiable layers in the Mars atmosphere. Extending from the surface are the troposphere, thermosphere and exosphere. A brief summary of the characteristics of each layer is provided.

The troposphere, extending from the surface to approximately 80 km, is characterized by a near linear decrease in temperature with altitude. The ceiling of the troposphere can vary in altitude depending on the amount of dust in the atmosphere. The four primary sources of information on the troposphere come from the surface measurements on the Viking 1 and 2 landers and Pathfinder mission and the Thermal Emission Spectrometer data from the Mars Global Surveyor, all of which provided reports of the surface conditions of the Martian surface [11, 12].

The coldest and least studied region of the Mars atmosphere is located in the altitude range of 80 to 120 km. This region includes the upper portion of the troposphere and the lower part of the thermosphere. The Viking and Pathfinder missions provided the only three in-situ measurements of the region of the atmosphere. However, with the M-01 aerobraking mission, further information will be obtained in this region.

Much of the information about the thermosphere, which extends from the 1.26 nbar pressure level (approximately 120 km) to approximately 230 km, was obtained from the MGS aerobraking mission. The 1.26 nbar level is the pressure at which the homogenous atmosphere of CO₂, N₂, Ar and H₂O begin diffusive separation. The thermosphere is characterized by an increase in temperature and density scale height with altitude. A full discussion of density scale height can be found in Section 1.3. The increased temperature is a result of the Extreme Ultraviolet, EUV, radiation that is converted to heat by dissociating molecules. EUV intensity is proportional to F10.7 which represents the 10.7 cm wavelength of the spectral line of hydrogen radiated from the Sun. F10.7 proves the closest surrogate representation of the amount of EUV radiation that is incident on a planet and is measured daily at the surface of the Earth. The value obtained on Earth is converted to obtain the amount incident on the planet Mars. The F10.7 daily variations are small, but over the 11-year solar cycle, the F10.7 value can range from approximately 40×10^{-22} to 140×10^{-22} W/cm² on Mars.

Finally, the exosphere, which extends from approximately 230 km is nearly isothermal and consists primarily of neutral particles but also of ions that have not yet escaped into space. Properties of this layer establish the evolution of the Mars atmosphere but have little impact on aerobraking missions.

The layers are more generally referred to as the lower atmosphere (troposphere) and the upper atmosphere (thermosphere and exosphere). As mentioned in Section 1.1, the density

obtained in the upper atmosphere depends on both heating in the lower atmosphere and the EUV heating in the upper atmosphere. The general circulation and interaction between the atmospheres is modeled for design and operations of aerobraking missions. Atmospheric models, used for operations and based on the characteristics of the lower and upper atmospheres, are discussed in detail in Chapters 2 and 4.

1.3 Mars Atmosphere as Experienced by Mars Global Surveyor

The atmospheric structure of Mars and characteristics that affect the atmospheric density have been reviewed. Since the M-01 aerobraking mission depends on the characterization of the density in the upper atmosphere, the time and location on the planet that the spacecraft will encounter are investigated and compared to the characteristics of the most recent aerobraking mission, MGS. This section reviews how density and scale height are obtained from the MGS mission. Then the properties of the MGS aerobraking orbits at periapsis are compared to the expected M-01 values.

The analysis of the MGS data focuses on the density of the atmosphere obtained from the spacecraft z-axis accelerometer. The drag acceleration in the z direction, which never deviated more than $\pm 15^\circ$ from the spacecraft velocity vector [3], is given by

$$a_z = \frac{\rho V^2 C_z A}{2m}. \quad (1)$$

In Equation 1 density is represented by ρ (kg/m^3), C_z , ranging from 2 to 2.2, is the force coefficient determined from an aerodynamic database over a range of spacecraft orientations to the relative wind, A is the cross sectional area of the spacecraft (17.03 m^2), m is the spacecraft mass (average 757.2 kg) and V is the magnitude of the spacecraft velocity relative to the atmosphere. The accelerometer measured counts. One count was equal to $0.332 \text{ mm}/\text{s}$ and could recover density to 3% at periapsis for nominal aerobraking altitudes [3].

Atmospheric density variability with altitude is determined by the density scale height, H_s , which, in the limit, is the altitude change over which the density decreases by a factor of e . Scale height is approximated from the models using density data above and below a reference altitude. For example, if the density was known at a reference altitude and a point 5 km above and below the reference altitude (see Figure 3) then the density scale height can be determined using

$$\rho_A = \rho_B e^{\frac{-(h_A-h_B)}{H_s}} \quad (2)$$

$$\rho_C = \rho_B e^{\frac{-(h_C-h_B)}{H_s}} \quad (3)$$

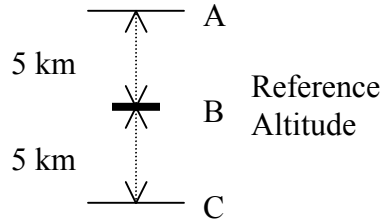


Figure 3. Scale height definition.

where ρ_A and h_A are the density and altitude, respectively at point A , and H_s is the scale height. The same applies for B and C . The equation for H_s obtained using Equations 2 and 3 is given by

$$H_{s_B} = \frac{-(h_A - h_C)}{\ln\left(\frac{\rho_A}{\rho_C}\right)} \quad (4)$$

The length of time an aerobraking mission will take depends on the density and the density scale height. Assuming that the spacecraft is flying at the same dynamic pressure or heating rate, then a larger H_s means the spacecraft will experience more integrated drag in the atmosphere per orbit thus reducing its speed and shortening the duration of the aerobraking

mission. Further explanation of scale height and its affect on the duration of an aerobraking mission can be found in Appendix A.

Figure 4 presents characteristics of the MGS aerobraking orbits at periapsis and the expected characteristics of the M-01 aerobraking orbits at periapsis regarding variations in altitude, latitude, season (L_s) and local solar time relevant to atmospheric modeling. The MGS data exists in two phases; Phase 1 (orbits<202) and Phase 2 (orbits>573). The discontinuity in the aerobraking orbits resulted because the spacecraft was placed in a science-phasing orbit to allow the final orbit to have the appropriate local solar time. Aerobraking resumed on orbit 574.

MGS aerobraking was conducted in the lower part of the thermosphere (110 to 170 km) except at the south pole where the altitude dropped to 100 km (see Figure 4a). However, the M-01 periapsis altitudes are expected to extend below 100 km. In addition to aerobraking at altitudes in which little is known about the atmosphere, the M-01 spacecraft is also expected to aerobrake at latitudes higher than the MGS mission. Figure 4a and 4b indicate that direct comparison of MGS data to M-01 cannot be made because many M-01 aerobraking orbits are expected to remain above 60° N latitude while the entire MGS aerobraking mission was performed below 60° N latitude.

Figure 4c shows a plot of the solar longitude, L_s , for both missions. The latter part of MGS Phase 1 ($L_s=270^\circ$ - 300°) does coincide with the L_s values of the M-01 mission. Hence the Phase 1 data are the most relevant to the M-01 season, but, again, these data do not extend above 60° N latitude and were obtained at altitudes approximately 20 km above the expected M-01 periapsis altitudes. However, the M-01 mission will be aerobraking over the north pole at winter ($L_s=265^\circ$ to 320°). If hemispheric symmetry is assumed, the M-01 expected data can

be compared to a portion of the Phase 2 data which occurred over the south pole at winter, allowing the characteristics of polar densities to be analyzed.

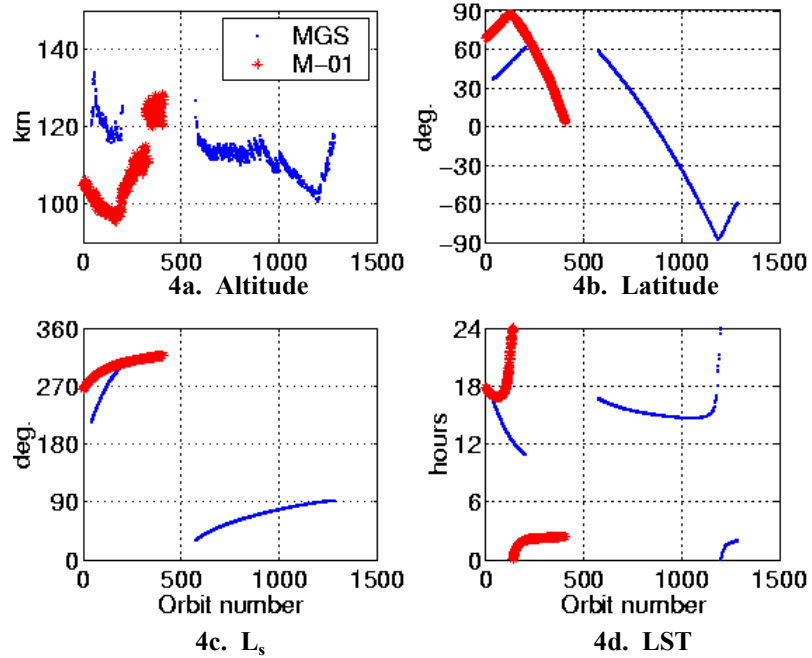


Figure 4. Properties of the MGS and M-01 aerobraking orbits at periapsis.

The L_s , at which M-01 will aerobrake, is important because it coincides with the dust storm season on Mars ($L_s=180^\circ$ to 320°) [8, 13]. The dust storm season on Mars occurs when the planet is at perihelion ($L_s \sim 250^\circ$) thereby maximizing the solar input on the planet. A look at Phase 1 data near orbit 50, which occurred in the dust storm season ($L_s=222^\circ$), provides data from a regional dust storm that developed in the Noachis region (40° S, 20° E) [9]. The effect of the storm on the density measured by MGS is seen in Figure 5. For the MGS mission, densities were derived at reference altitudes (i.e., 120 km, 130 km, 140 km, etc.). Figure 5 shows inbound and outbound density data at a reference altitude of 140 km versus time in days from orbit 40. This data was obtained during the storm. The density increases from an average of about 1.5 kg/km^3 for orbits in the late 40's to almost 5 kg/km^3 on orbits 55 and 56 then exponentially decays. The time elapsed for the storm to decay by a factor of e for the inbound high northern latitude data after orbit 80 (approximately 50 days from orbit 40) was

approximately 60 days. However, the exponential decay of the outbound lower latitude data was approximately 80 days. The longer decay time for the outbound data obtained at lower latitudes results because the storm originated in the southern hemisphere. It should be noted that the M-01 mission is scheduled to begin aerobraking operations during the peak dust storm season.

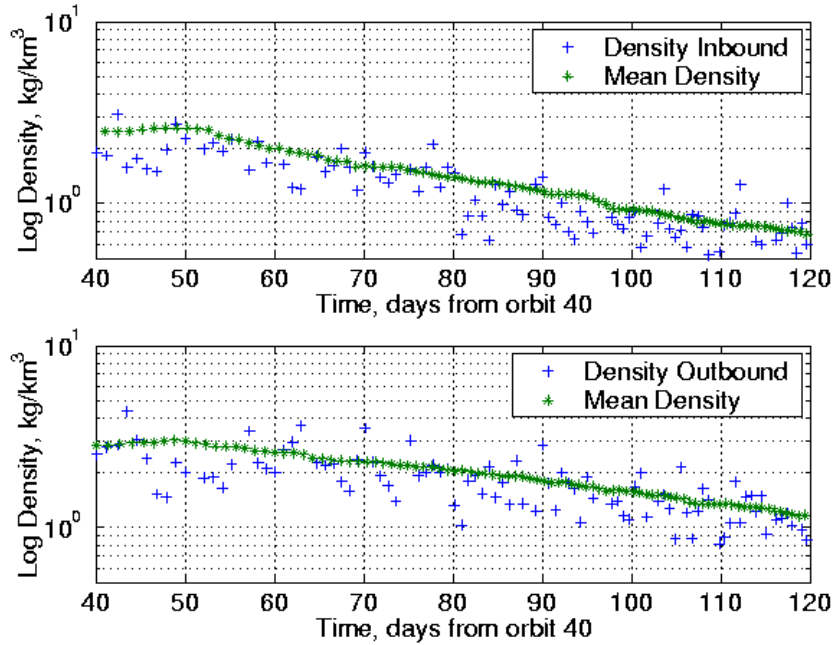


Figure 5. Phase 1 inbound and outbound log densities at 140 km versus time.

The expected LST for the M-01 mission at periapsis during aerobraking is between 1600 and 0200 hours (4 P.M. to 2 A.M.) as seen in Figure 4d. MGS Phase 2 provides thorough coverage of this LST range. For a satellite in a nearly polar orbit, diurnal variations are difficult to separate from other variations. However, a strong day-night effect was detected at the south pole late in the MGS mission [14]. Therefore, except for the hemispheric difference, Phase 2 provides the conditions most similar to the expected M-01 conditions.

The main characteristics of the MGS mission, regarding altitude, latitude, L_s , LST and dust storms, have been established and compared to the expected values for the M-01 mission.

Despite occurring during the same season expected by M-01, MGS Phase 1 data does not correspond in latitude, altitude or LST. However, MGS Phase 2 data, which occurs during similar LST, also provides polar density data that may apply to the M-01 mission. Understanding the atmospheric characteristics of the MGS mission allows extrapolation to the M-01 mission. The MGS characteristics have been incorporated into current models of the Mars atmosphere to allow the most accurate predictions of atmospheric density and scale height. One such model is the Mars Global Reference Atmospheric Model, Mars-GRAM [15], discussed in Chapter 2. The accuracy of the Mars-GRAM in reproducing MGS data is presented in Chapter 3.

Chapter 2. Current Models of the Mars Atmosphere

The success of aerobraking depends on how well atmospheric models capture the effects of variations in season, LST, latitude, longitude and dust storms. Models of the Martian atmosphere evolve with each mission to the planet. One of these evolving engineering-oriented models is the Mars Global Reference Atmospheric Model, (Mars-GRAM), developed by Johnson *et al.* (1989) and Justus (1990 and 1991). Mars-GRAM incorporates all the atmospheric variables discussed in Chapter 1 to calculate the mean and wave perturbed atmospheric density for any location (altitude, latitude, and longitude) and time (seasonal and diurnal) on the planet [16]. The location and time parameters are input into the Mars-GRAM program *namelist* by the user. The original version of Mars-GRAM was released in 1989, and since then the program has been updated numerous times.

Mars-GRAM uses tables from General Circulation Models, GCMs, as an atmospheric data base. GCMs “explicitly simulate large-scale atmospheric flow, and parameterize a wide range of physical processes active in the climate system, such as radiative transfer, surface-atmosphere interactions and the effect of unresolved turbulent mixing and transport” [17]. The GCM results are directly dependant on the surface features of Mars. Two different atmospheric models are used in Mars-GRAM to calculate the density in the layers of the atmosphere described in Section 1.2.

The lower atmosphere (surface to 90 km) uses the Mars General Circulation Model (MGCM) developed at NASA Ames Research Center [18].

“The MGCM is a primitive equation, grid-point numerical model of the Martian atmosphere. It contains a variety of numerical parameterizations for the treatment of such physical processes as radiative transfer (solar absorption and infrared absorption and emission by gaseous CO₂ and suspended dust), atmospheric/surface interactions (transfer of momentum and sensible heat),

condensation/sublimation of carbon dioxide (and the concurrent changes in atmospheric mass), and imposed flow deceleration near the top (for both physical and numerical reasons).”

The thermospheric model (80 km to 170 km), in recent versions of Mars-GRAM, uses the National Center for Atmospheric Research (NCAR) Mars Thermosphere General Circulation Model (MTGCM) [18].

The MTGCM “has been adapted to the unique fundamental parameters, physics and inputs appropriate to the Mars upper atmosphere... The code itself is a finite-difference primitive equation model that self-consistently solves for steady-state or local-time dependent temperatures, densities and 3-component winds over the globe. The MTGCM physics is firmly based on well studied CO₂ energetic and chemical processes for Venus that should apply to Mars as well.”

Above 170 km, Mars-GRAM uses an empirical Stewart model [19] to describe the upper atmosphere, however the densities at these altitudes have little effect on aerobraking missions and will not be discussed in detail.

Mars-GRAM is frequently used in mission and spacecraft design. In particular, versions 3.7 and 2000 of Mars-GRAM are being used for the M-01 mission. Mars-GRAM 3.7 (released in 1997) was used to design the M-01 mission and Mars-GRAM 2000 (released 2000) has been selected for M-01 aerobraking operations. The reason for the version upgrade is detailed in Chapter 3 and lies in the fundamental differences between the two versions, which are outlined briefly here.

2.1 Mars-GRAM 3.7

The original version of Mars-GRAM (1990) was based on surface and atmospheric temperature data obtained during the Mariner and Viking missions and on surface pressure data collected by the Viking landers [15]. However, recent observations indicate that the atmosphere has cooled in the decades since these missions [15, 20]. For this reason, climate factors, CFs, were included as inputs to Mars-GRAM 3.7 (MG3.7). An example of the *namelist* of inputs for MG3.7 is provided in Appendix B. Inclusion of the CFs allows the user

to incorporate the effect of temperature changes since the 1970's for the lower atmosphere (surface to 75 km). Allowing for the temperature change effectively alters the pressure and density produced by MG3.7 at the lower altitudes.

In MG3.7 the region of the thermosphere between 80 and 170 km is modeled using only four sets of outputs from the MTGCM. The four sets are used to find the thermospheric parameters as functions of latitude, sub-solar latitude and LST [15].

2.2 Mars-GRAM 2000

The major difference between Mars-GRAM 3.7 and Mars-GRAM 2000 (MG2K) is that MG2K replaces the data-derived parameterizations of the atmosphere (used in MG3.7) with higher resolution data tables from the MGCM for the lower atmosphere and MTGCM for the thermosphere. The use of the data tables in MG2K eliminates the need for the climate factors used in MG3.7. Another MG2K improvement includes the option to input background dust levels that exist near the surface, while still allowing the user to input the location, size and intensity of a dust storm as in previous versions.

During the MGS aerobraking mission, standing density wave phenomena was observed in the atmosphere [10]. For this reason, MG2K also includes a longitude-dependent (terrain fixed) wave (LDW) model. After determining the mean density from the MGCM and MTGCM data tables, MG2K allows the user to include an offset to the mean density as well as wave numbers one through three (i.e., wave number 2 means that two wavelengths encircle the planet) from the equation

$$LDW = B_o + B_1 \cos[\pi(\lambda - \Phi_1)/180] + B_2 \cos[\pi(\lambda - \Phi_2)/90] + B_3 \cos[\pi(\lambda - \Phi_3)/60]. \quad (5)$$

Based on Equation 5, the user can adjust the mean density by specifying a mean density wave perturbation offset, B_o , (namelist input *WaveA0*), amplitude, $B_{1,2,3}$, (*WaveA1*, *WaveA2*, and

WaveA3) and phase, $\Phi_{1,2,3}$, (*Wavephi1*, *Wavephi2*, and *Wavephi3*) for wave components 1, 2 and 3 of the stationary longitude (λ) dependent waves [13]. The namelist for all inputs to MG2K is provided in Appendix B. Since significant wave activity was observed during the MGS mission, this version offers greater flexibility for modeling the atmosphere during future aerobraking operations.

Now that the fundamental differences between the Mars-GRAM versions have been outlined, Chapter 3 includes the analysis performed to determine the effects of the differences on aerobraking parameters.

Chapter 3. Comparison of Mars-GRAM to MGS Data

The M-01 mission was designed using MG3.7. However, since the spacecraft was built, a more recent version of the atmospheric modeling software, MG2K has been released. The new version incorporates more atmospheric information based on knowledge gained from the MGS mission. Therefore, it was of interest to determine if using the data derived parameterizations in MG3.7 or the high-resolution data tables in MG2K more closely represented MGS data and should be used for aerobraking operations and simulations of the M-01 mission.

The performance of both versions was distinguished by how accurately each could reproduce MGS density and scale height measurements. MGS altitude, latitude and longitude information at periapsis were used in both versions to obtain the corresponding density. A ratio of the MGS density to the Mars-GRAM density was obtained for comparison using

$$\text{Ratio} = \frac{\text{MGS density at periapsis}}{\text{Mars-GRAM density at periapsis}}. \quad (6)$$

Scale heights in Mars-GRAM were calculated using the method outlined in Section 1.3 and Equation 4. The comparison of MGS density and scale height data to MG3.7 and MG2K calculated density and scale height is now presented.

3.1 Comparison of Mars-GRAM 3.7 with MGS Density Data

Figure 6 is a plot of the density ratios from Equation 6 versus orbit number for a nominal dust case (namelist input $CFs=1$) using MG3.7 [21]. Both Phase 1 and 2 exhibit ratios below 4, except between orbits 1070 and 1270. Those 200 orbit periapses are located poleward of 60° south latitude. Orbit 1200 corresponds to when the spacecraft passed closest to the south pole of Mars. For completeness the full range of ratios is shown in Figure 7.

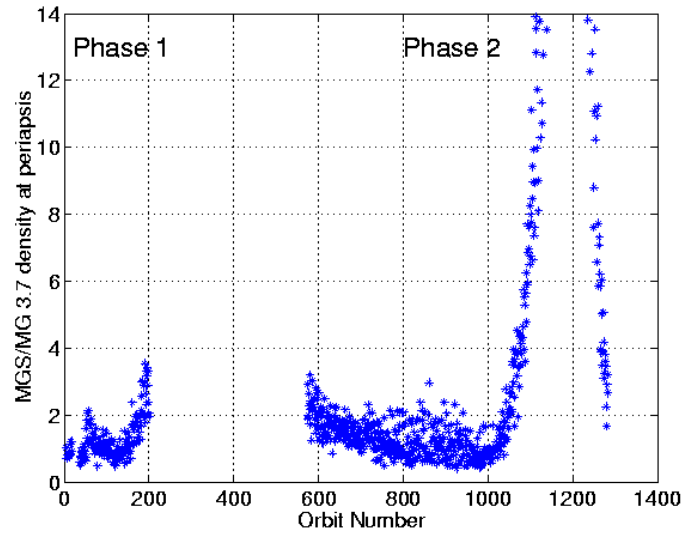


Figure 6. Ratio of MGS data to MG 3.7 predicted data for the nominal dust case.

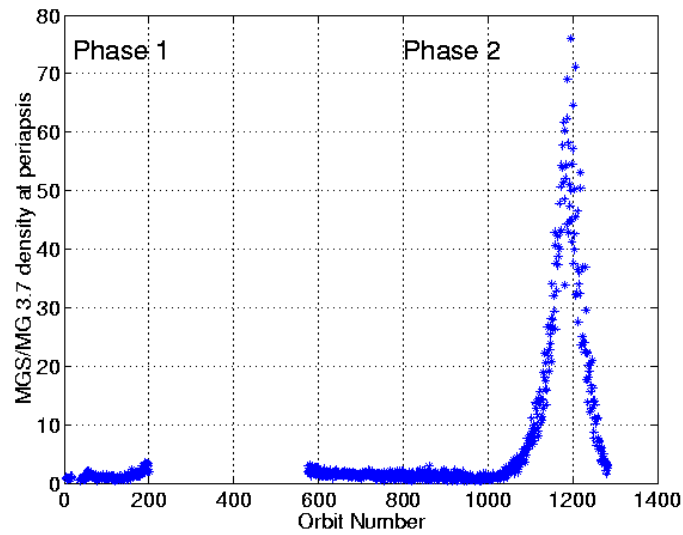


Figure 7. Ratio of MGS data to MG 3.7 predicted data (complete range).

The significant increase in ratios near orbit 1070 may be caused by an overestimation of the latitudinal density gradient in MG3.7 near the pole. The Mars-GRAM MTGCM density predictions are plotted with MGS density for Phase 1 and 2 versus latitude in Figure 8 [22].

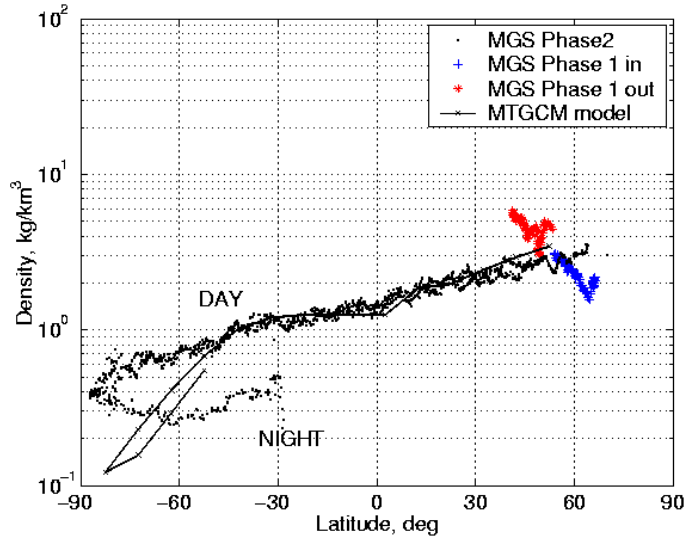


Figure 8. Density at 130 km versus latitude for MGS data including Phase 1 and 2.

The downward slope of the MTGCM line near the south pole (poleward of -60°) in Figure 8 is evidence of an overestimation of the latitudinal gradient found in the model compared to the MGS Phase 2 averaged inbound and outbound data in the same region. Phase 1 data for both inbound (*in*) and outbound (*out*) orbits 110-201 at reference altitude 130 km, which exclude major dust storm effects, are also plotted in Figure 8 and appear to exhibit a similar strong gradient near the north pole that the MTGCM shows at the south pole. This may suggest different latitudinal density gradients exist during the winter at both poles.

3.2 Comparison of Mars-GRAM 2000 with MGS Density Data

Ratios of MGS densities to MG2K densities were also obtained and graphed versus orbit number. As mentioned in Section 2.2, MG2K offers an improvement over MG3.7 because it allows for more accurate distribution of the dust in the atmosphere. This is accomplished in MG2K by specifying the input parameter, *Dusttau*, to specify background atmospheric dust. *Dusttau* represents the dust opacity of the atmosphere, which as mentioned in Section 1.1, can range from zero to three. MG2K, as with earlier versions, also retains the

capability to define the intensity and location of a dust storm through the input parameters *INTENS* and *ALSO*. However for the first comparison of the model to MGS data only the nominal dust case was considered (i.e. no dust storm was simulated and *Dusttau*=0.3). Figure 9 depicts the ratio for the MG2K nominal dust case. It can be seen that MG2K underpredicts the MGS density by as much as a factor of 12 for Phase 1. This compares to ratios less than 4 observed with the MG3.7 model of the same phase, while the MG2K Phase 2 ratios near the pole (orbit 1200) are much lower (~10) compared to those obtained using MG3.7 (~76) in the same region.

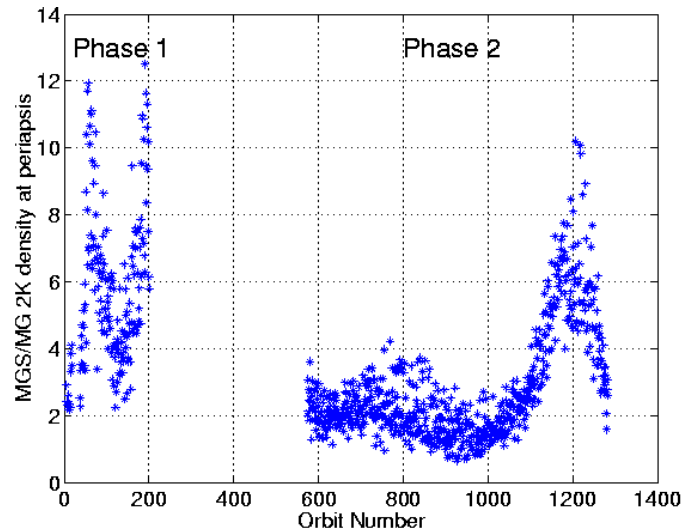


Figure 9. Ratio of MGS to MG2K data for the nominal dust case.

In an attempt to improve the ratios for Phase 1, the regional dust storm that began in the Noachis region, which occurred near orbit 50, was included in MG2K. The dust storm was included into the namelist inputs of MG3.7 and MG2K by specifying the location, season (*ALSO*), intensity (*INTENS*) and maximum radius of a dust storm. *Dusttau* was also specified in MG2K to provide a background dust level. Since ratios produced using MG3.7 are already near unity for Phase 1 the analysis was performed using only MG2K. The inputs and values for

the three parameters that affect density during a dust storm in MG2K, and used in the analysis, are found in Table 1 [23]. The table lists the values for the nominal and dust storm cases. Referring to the data in columns 4 and 5, Phase 1 included a location and intensity of the dust storm while Phase 2 only used a slightly higher background dust content to mark the remaining dust in the atmosphere resulting from the regional dust storm.

Table 1. Input Values to Account for the Dust Storm in Mars-GRAM 2000.

Namelist Input	Nominal Dust		Dust Storm	
	Phase 1	Phase 2	Phase 1	Phase 2
Dusttau	0.3	0.3	0.4	0.5
ALSO (deg)	0.0	0.0	222	0.0
INTENS	0.3	0.3	0.6	0.0

Changing the three parameters for each Phase produced the ratios seen in Figure 12. Note that the ratio of densities drops from a maximum near 12 in Figure 9 to a maximum near 10 in Figure 10 for Phase 1 and from a maximum ratio of 10 to 6 for Phase 2.

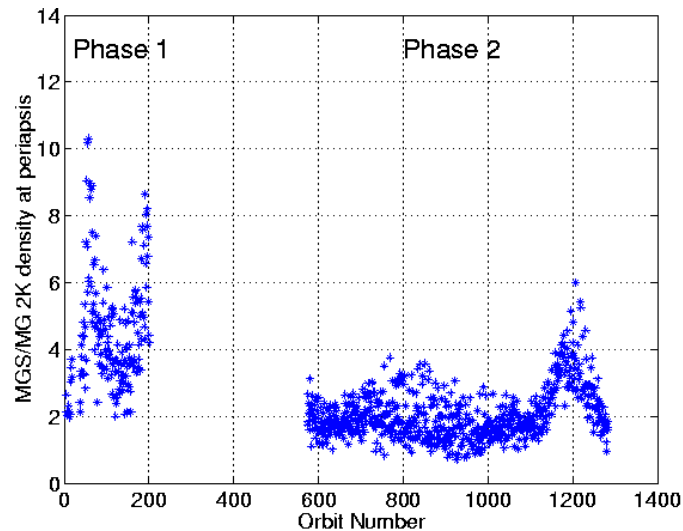


Figure 10. Ratio of MGS to MG2K data for the dust storm case.

The result of changing dust storm parameters to differentiate between the dust storm and background dust level, as seen in the differences between Figures 9 and 10, illustrates the

sensitivity of MG2K to input dust conditions. MG3.7 required no adjustment to the inputs to obtain ratios near unity during the Phase 1 dust storm. Based on the nominal dust case, MG2K is significantly better at predicting densities within 30° of the south pole, while MG3.7 provides better predictions of the MGS atmospheric density for the overall duration of the mission.

3.3 Comparison of Scale Heights

Another difference between MG3.7 and MG2K was realized during prelaunch M-01 aerobraking mission simulations. Concern arose when simulated aerobraking durations using MG3.7 were up to 40% shorter than those obtained using MG2K. To establish an acceptable launch window, it was important to determine which version more accurately represented the atmosphere of Mars. Studies indicated that a portion of the discrepancy in aerobraking duration could be explained by the difference in the scale height calculated by each version. An analysis was performed using MGS data to determine the magnitude of the effect. MGS parameters at periapsis were input into each version of Mars-GRAM to obtain densities. The H_s was calculated as described in Section 1.3 using Equation 4. As seen in Figure 11, MG3.7 produced higher scale heights than MG2K which would result in a shorter aerobraking mission.

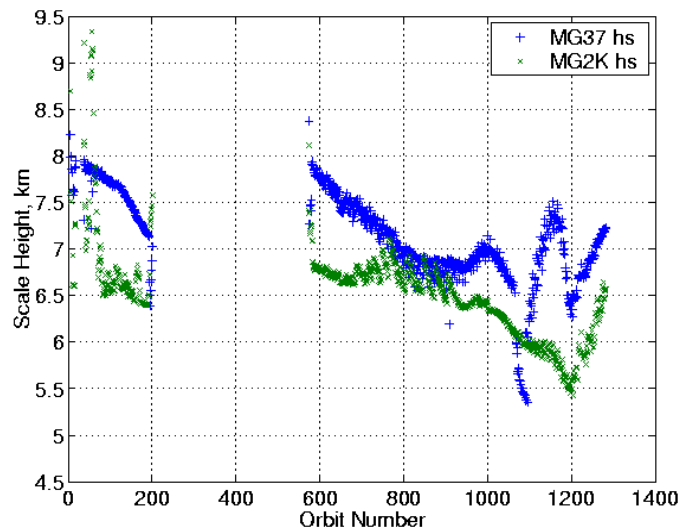


Figure 11. Scale height calculations of MGS data from MG3.7 and MG2K.

The difference in H_s is approximately 1 km at an average altitude of 114 km. A 1 km difference will not cause a 40% reduction in aerobraking duration. However, the M-01 mission is expected to aerobrake at altitudes approximately 10 to 20 km lower than MGS, in a region of the atmosphere that is uncharted. Aerobraking at lower altitudes presumes that the spacecraft will encounter lower scale heights. If the H_s calculated in MG3.7 produced a number much greater than the H_s produced in MG2K at the same lower altitudes, the 40% reduction in aerobraking duration would be explained. This prompted a second analysis. MGS altitudes were reduced by 10 km and used in both Mars-GRAM models to determine the difference in calculated H_s at the lower latitudes. The results can be seen in Figure 12.

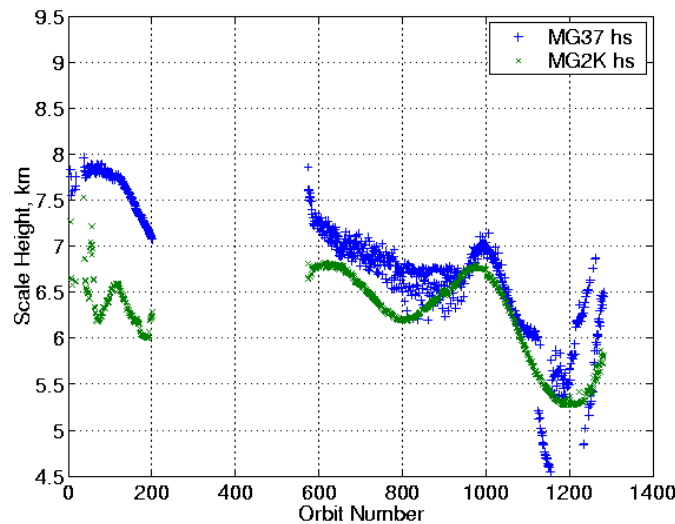


Figure 12. Scale height calculations using MGS data at lower altitudes.

At lower altitudes, the calculated scale height difference between the Mars-GRAM versions is greatest in the high northern latitudes (orbits 0 to 200 and 574 to 700). While the difference in the calculated scale heights will result in different aerobraking mission durations, the difference is not enough to cause a 40% reduction.

3.4 Lessons for the Mars 2001 Mission

The purpose of the density and H_s investigations was to explore the differences between MG3.7 and MG2K and to evaluate the impact of these differences on the M-01 aerobraking profile. Recall from Section 1.3, the atmosphere encountered by MGS was compared to that expected by M-01. The section reviewed the factors that affect the density of the atmosphere: altitude, latitude, season, LST, and atmospheric dust. It was noted that the entire MGS mission occurred at higher altitudes and lower latitudes in the Northern Hemisphere than is expected for the M-01 mission so no direct comparisons of data can be made. However, the Phase 1 orbits 100-200 were closest in season to M-01 and the Phase 2 winter polar orbits (1070-1270), which are similar to the atmospheric conditions expected, are the most similar in latitude to the M-01 mission. Therefore, particular focus was given to analysis of the ratios of MGS density to Mars-GRAM density for both versions in these regions.

The analysis of the MGS Phase 1 orbits 100-200 to MG3.7 nominal dust ($CF's=1$) comparisons (Figure 6) yielded density ratios that ranged from 1 to 4, while MG2K ratios for the nominal dust case ($Dusttau=0.3$) in the same region yielded ratios ranging from 2 to 12. Therefore MG3.7 performed better (by almost a factor of three) than MG2K during this season ($L_s=270^\circ$ to 300°). Analysis of the MGS to MG3.7 ratios in the polar region (orbits 1070-1270) was near 75 for the nominal dust case while the MGS to MG2K ratios for the same region were near 10. In this case MG2K performs better (by almost a factor of 7.5) compared to MG3.7.

The significantly large ratios produced using MG3.7 at the pole compared to those produced using MG2K raised concern as to the validity of using MG3.7 for M-01 aerobraking operations which are expected to encounter similar winter polar densities. The ratio differences between MG3.7 and MG2K data of similar season (orbits 100-200), where MG3.7 predicted closer densities, were not nearly as large as the ratios differences experienced in the polar

region. Additionally, as mentioned in Chapter 2, MG2K allows for input of stationary atmospheric waves, explained in Chapter 1 and experienced by MGS, to be included in the model. The wave model in MG2K is advantageous for modeling the variability of the atmosphere during aerobraking operations and simulations of missions.

Better prediction capabilities at the south pole, the inclusion of the wave model and higher resolution data tables in MG2K were all factors that influenced the decision to recommend MG2K for the M-01 Odyssey atmospheric model. The scale height analysis had little impact on the selection of the Mars-GRAM version. MG2K has subsequently been accepted by the M-01 Atmospheric Advisory Group for operations and simulations of the mission.

3.5 Improving Comparisons With Mars-GRAM 2000

Since MG2K offers greater flexibility for modeling the atmosphere and provides better agreement with MGS data in the polar region over MG3.7, attempts were made to reduce the density ratio of MGS to MG2K data. Improvement was obtained by modifying the inputs to MG2K. The first modification to the MG2K input was the inclusion of a MGS data derived wave model. The derivation of the wave model is provided in Chapter 4. The second improvement was the inclusion of an altitude offset (h_{off}) as a function of season. The effects of both modifications are explored.

The wave model was created as a means of simulating variations in the mean density, and phase and amplitude of Mars atmospheric waves in MG2K. The model uses a 30 orbit running least squares solution of MGS densities at periapsis to identify the systematic variations of the phase and amplitude in waves numbers 1, 2, and 3 with latitude. The parameters are entered in the MG2K *namelist* and used according to Equation 5. The wave

model was also developed with a distribution on the mean density term to capture the random variability in the atmosphere. However, for this study only the reference wave model was used (i.e., no variations were imposed on the mean density or the phase and amplitude of the waves). The reference wave model phase and amplitude data comprise a table that is linearly interpolated in latitude. Figure 13a shows the density ratios versus orbit number when the wave model is included in the input to MG2K. When comparing Figure 13a to Figure 9, the addition of the wave model reduces the scatter of the ratios but does not reduce the magnitude significantly.

To obtain a reduction in the magnitude of the ratios of MGS to MG2K (i.e., to bring the MG2K calculated densities to closer agreement with MGS measured densities), a second modification was made to the altitude input. The empirical altitude offset as function of season, which allowed MG2K to better match observed data, is given by [24]

$$h_{off} = 5 - 2.5\sin(L_s). \quad (7)$$

Since the densities obtained from the MG2K are less than the atmospheric densities measured by MGS, h_{off} is subtracted from the altitude input to MG2K, producing the results shown in Figure 13b. The ratios are significantly reduced using h_{off} compared to the ratios found in Figure 9. Figure 13c is a plot of the density ratio versus orbit number when both the wave model and offset are applied in the MG2K inputs.

In an effort to further reduce the density ratios, the dust storm parameters from Table 1 were included in the input to MG2K. The results are shown in Figure 14. Figure 14c illustrates that the dust parameters and the two modifications result in ratios for both MGS Phases below 4.

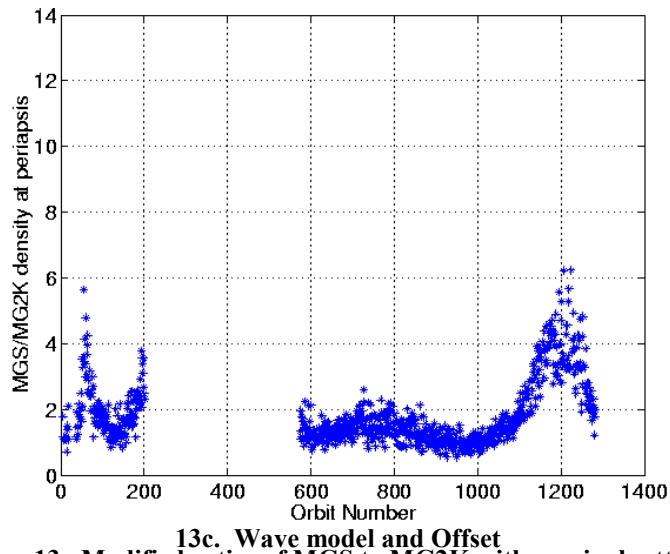
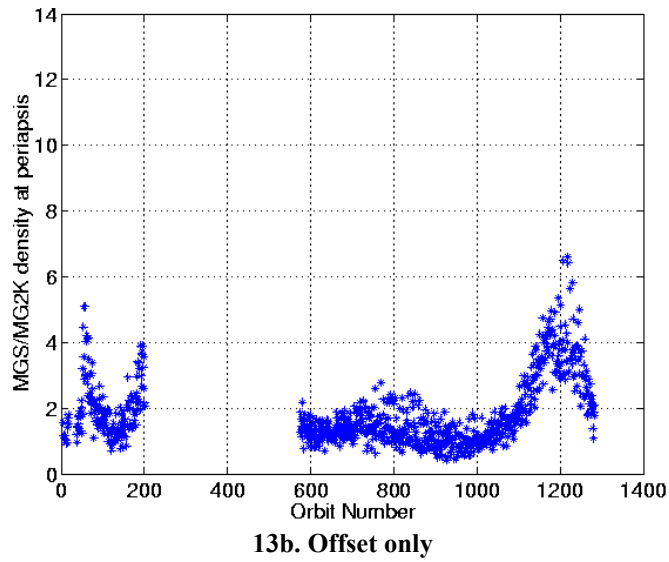
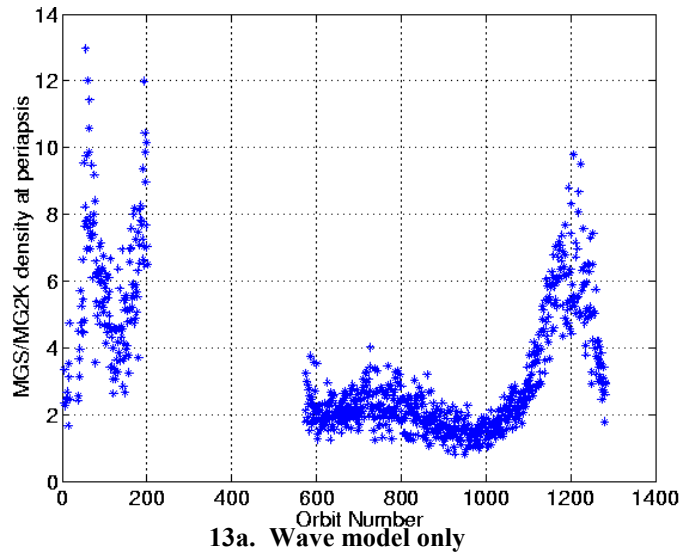
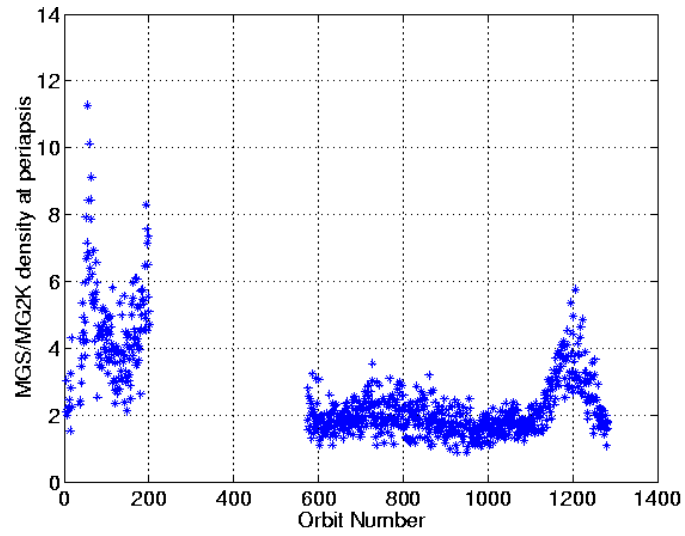
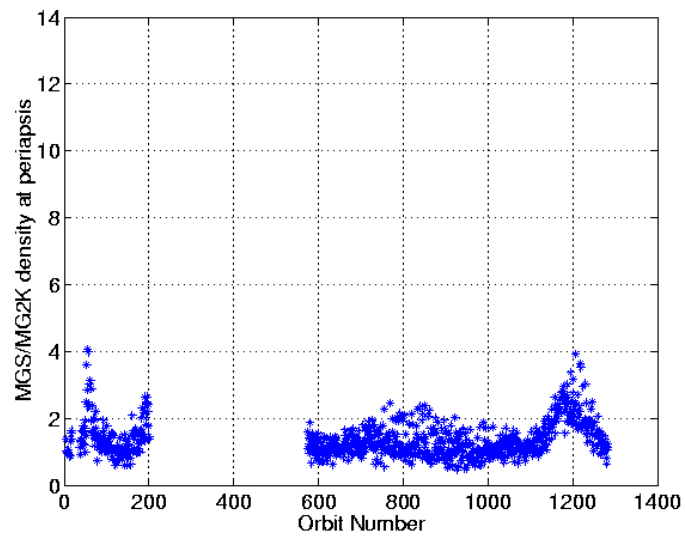


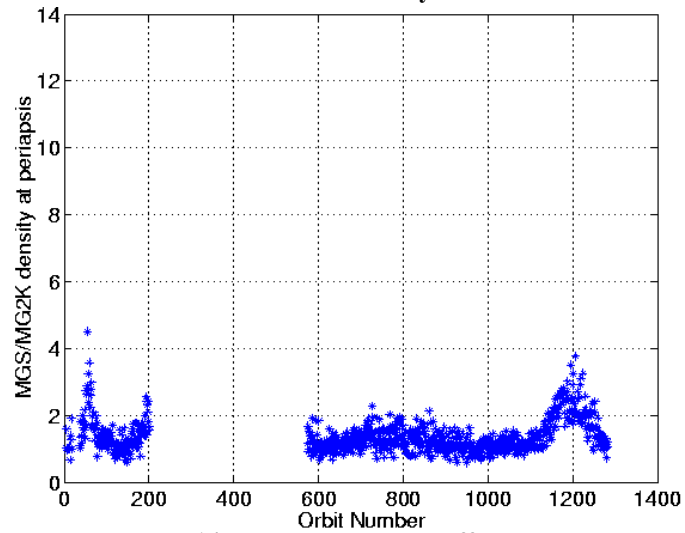
Figure 13. Modified ratios of MGS to MG2K with nominal settings.



14a. Wave model only



14b. Offset only



14c. Wave model and offset

Figure 14. Modified ratios of MGS to MG2K with dust storm settings.

Since the amount of dust in the atmosphere will not be known until aerobraking begins, further analysis was performed using MG2K without the dust parameters from Table 1 to obtain the characteristics of using the modified inputs. A seven point running mean (μ) and standard deviation (σ), shown in Figure 15, was calculated for the ratios obtained by using the offset and the wave model from Figure 13c.

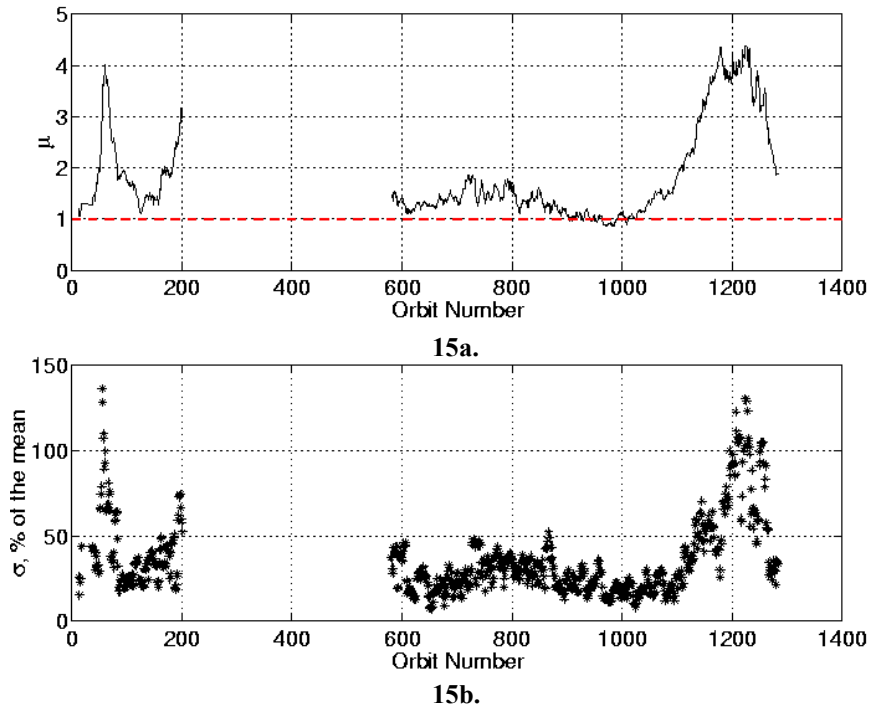


Figure 15. Seven point running mean of the wave model and offset; sigma for each mean.

Figure 15a shows the remaining signal and underlying bias in the estimates, especially during the dust storm (orbit 50) and near the south pole (orbits 1070-1270). Including the offset in the model attempted to reduce the bias. The average deviation of 30% for the majority of the MGS aerobraking mission, shown in Figure 15b, illustrates the unmodeled variability in the atmosphere. The larger sigmas result from the dust storm which occurred near orbit 50 and an underestimation of the density by MG2K in the polar region (near orbit 1200).

In a second analysis, the density ratios from Figure 13c are plotted versus latitude instead of orbit number. The result, shown in Figure 16, suggests that a latitudinal gradient

exists in MG2K, similar to MG3.7 (Figure 8), which begins near 60° N and extends poleward. The gradient appears to be stronger in the northern hemisphere, previously noted in the MGS Phase 1 data found in Figure 8, and has an impact only on winter poles. The peak in the ratios of Phase 1 data near 40° N latitude (Figure 16) is due to the Noachis dust storm. The deviation from the mean density and the effects of the latitudinal gradient are important to consider when analyzing the results of the MG2K density predictions of the M-01 mission since the majority of aerobraking will occur poleward of 60° N latitude.

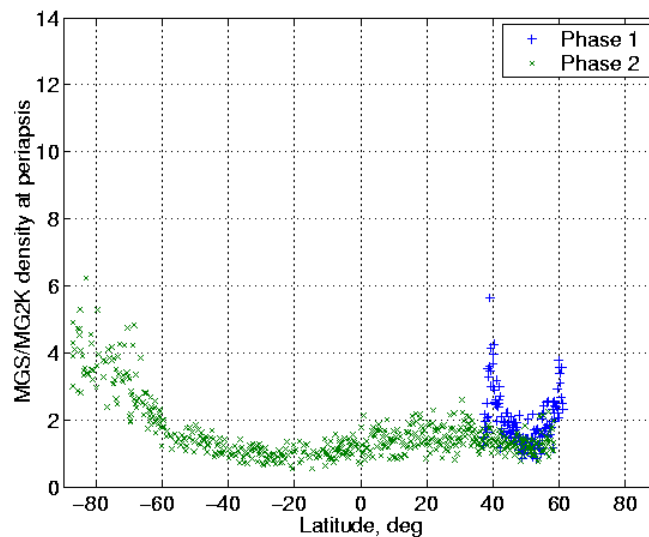


Figure 16. Ratio of MGS to MG2K densities at periapsis versus latitude, nominal settings.

The inclusion of the altitude offset, the wave model and the dust storm effects to MG2K significantly improved the density ratios of the entire MGS data set, especially in the polar region (orbits 1070 to 1270) from the values seen in Figure 9. Therefore, implementing of the modifications make it possible to obtain densities comparable to those obtained during MGS aerobraking mission. This analysis prompted the release of an upgraded version of MG2K specifically for the M-01 mission known as the MG2K Odyssey version. The upgraded version included the altitude offset as an input option in the program *namelist*.

Chapter 4. Monte Carlo Modeling Methods

Monte Carlo (MC) simulations are performed for planetary missions to study the statistical probabilities of particular mission characteristics such as aerobraking mission duration and fuel requirements. Monte Carlo simulations for aerobraking missions attempt to account for all uncertainties that effect aerobraking including atmospheric, aerodynamic, gravitational, and solar pressure variations to obtain the most accurate simulations. The most dominate uncertainty in aerobraking mission simulations lies in the atmospheric variability. As mentioned in Sections 1.1 and 2.2, large systematic planetary waves were observed on Mars by MGS, however a large amount of unmodeled variability also exists in the atmosphere. Therefore, utilizing the large amount of MGS atmospheric data, which allowed for the first statistical analysis of the Mars upper atmosphere, a model is proposed which captures both the systematic and random variations in the atmosphere of Mars for MC simulations of the M-01 aerobraking mission.

The thermal margins of the MGS mission were based on a 70%- 2σ orbit-to-orbit variation in periapsis atmospheric density. During aerobraking operations, this variability estimate was validated with flight data. After orbit 15, thermal loading was not an operational consideration as attention turned to limiting the maximum dynamic pressure during each pass [25]. Numerous methods were attempted to predict atmospheric density at subsequent orbits based on past data [3]. Persistence, predicting the density at orbit $n+1$ based on the observed density and H_s at orbit n , resulted in prediction errors of about 40%- 1σ . Five orbit running means of density improved the prediction capability to 30% [3]. A stationary wave model provided single orbit prediction to about 25% and also provided reasonable prediction for a

week or more. The wave model predictions were used in a qualitative way to make maneuver decisions.

Because of the limited pre-flight knowledge of the atmosphere, no known attempts were made to perform pre-flight MC simulations of MGS operational maneuver strategies based on atmospheric variability. Simply modeling the atmosphere as a nominal with 35%-1 σ Gaussian variation may have resulted in excessive restrictions on operations or excessive requirements on the spacecraft. However, the knowledge of the thermosphere provided by MGS enables more realistic simulations of aerobraking operations for the M-01 mission. This chapter proposes a method and wave model for use in the selected version of Mars-GRAM, MG2K [13], for M-01 MC simulations of the aerobraking phase. The model is based on MGS aerobraking results, the most recent in-situ measurements of the atmosphere of Mars. Consequently, two major caveats must be kept in mind. First, the latitudinal-seasonal space to be sampled by M-01 is not completely covered by the MGS data set, so extrapolation (a generally dangerous procedure when dealing with natural phenomena) is required. Second, the MGS mission provides “one sample” of the Mars thermosphere and there is no guarantee the “same” atmosphere will be repeated in latitude and season space. One known difference is that M-01 will occur near solar activity maximum while MGS was just after solar minimum. This difference has a negligible effect at aerobraking altitudes in the thermospheric models used by the project. The effect on the real atmosphere is unknown, but expected to be small and essentially a slowly varying bias in density that will be readily absorbed in the operational density prediction schemes.

With these caveats in mind the MC model includes (1) a reference model, utilizing the stationary wave capability in MG2K, to be used for nominal mission design, (2) a statistical deviation from the reference model for MC simulations, and (3) development of a wave model

using density results obtained from MGS accelerometer data. From analysis of MGS data in Section 1.3, emphasis is on the high northern hemisphere, winter (Phase 1) data, but with some weight given to high southern hemisphere, winter (Phase 2) data.

4.1 Monte Carlo Simulation Overview

Monte Carlo simulation of the entire aerobraking phase is performed numerous times to obtain a “mean” mission and deviations from the “mean.” The development of the MC wave model involves determining the statistical variation of the atmosphere only. The following methodology is suggested for the MC wave model:

1. For each mission simulation, select random dust storm characteristics, e.g., select the value of L_s at which the dust storm is to begin. Also select random optical depth, intensity, size, location, and any other parameters required to define a dust storm in MG2K. The MG2K model of the dust storm will be invoked in the simulation with the selected parameters. Probability distribution functions (PDF) for dust storm parameters are not developed herein, but for example, the beginning of the storm might be uniformly distributed between $L_s=180^\circ$ and 320° or, as observations indicate, a higher probability density could be associated with L_s around 270° .
2. Beginning with the walk-in phase, generate a random atmosphere for each aerobraking pass from the distributions proposed in Section 4.2 and Section 4.3.
3. Perform periapsis up or periapsis down maneuvers based on maneuver strategy.
4. Continue to the end of the aerobraking phase.
5. Go to 1 until mission statistics converge. Statistics might include total maneuver change in velocity or total aerobraking duration.
6. Evaluate maneuver strategy and mission success criteria.

4.2 Planetary Wave Models

MGS aerobraking data have been utilized to identify a number of differences between observations and the thermospheric theoretical model upon which MG2K is based. For example, as discussed in Chapter 3, measurements near the south pole suggest a much smaller latitudinal density gradient than predicted by the theoretical model. Though important from the scientific viewpoint, such deviations will have little impact on operations, since operational

procedures to predict density for future orbits should accommodate latitudinal gradients. The difference that could most affect operations was the discovery of what appeared to be stationary waves in the thermosphere. These waves can produce 100% deviations in density from trough to crest. The waves appear to be global in nature and appear to persist for periods of time comparable with the duration of the M-01 aerobraking phase. Scientific analysis [26] suggests that Kelvin waves, which are equatorial and travel eastward around the planet in 1 sol, may be the mechanism behind one of the observed waves. To a polar orbiting satellite, such a wave might appear as a stationary wave with wave number 2 (i.e., wave number 2 means that two wavelengths encircle the planet). Due to persistence, the global nature of the waves, and the density ratio extremes, it is desirable to consider such waves in the reference model for defining the “nominal” mission and in the MC simulations. Recall that one of the main rationales for proposing MG2K as the reference model for the mission is that MG2K permits the inclusion of stationary waves with wave numbers 1, 2 and 3.

4.2.1 Mars-GRAM Wave Model

In developing the models, a generalized form of Equation 5 was used for the wave model given by

$$\rho(h, \phi, \lambda) = \rho_o(h, \phi) \left[A_o + \sum_{n=1}^3 A_n \sin(n(\lambda - \lambda_n)) \right] \quad (8)$$

where ϕ is latitude, λ is East longitude, h is altitude above the reference ellipsoid and ρ_o (similar to B_o from Equation 5) is the MG2K density at the specified location. A_n (similar to $B_{1,2,3}$) is the amplitude as a fraction of ρ_o and $0 < \lambda_n < 2\pi/n$ (similar to $\Phi_{1,2,3}$) is the phase of wave number n stationary-longitudinal wave. The phase is the traditional longitude going from negative to positive. The phases in Equation 8 are readily converted to the MG2K form of

Equation 5 by adding 90° to the phase of wave 1, 45° to the phase wave 2 and 30° to the phase of wave 3. A_o provides a term to scale the MG2K density. In MG2K, ρ_o is also a function of season (L_s) and local solar time (LST). The latter is included in the diurnal and semi-diurnal tides terms [13]. For near polar orbits, the tidal contributions vary slowly except when the periapsis is near the pole. In this case, the satellite can pass from day to night and experience a larger tidal contribution. This would be noticeable for low eccentricity orbits. Above about 125 km altitude, the atmospheric density in MG2K also varies with solar activity. The EUV flux, which heats the thermosphere, is included in MG2K through the surrogate F10.7 cm flux. MG2K automatically includes solar activity and tides in ρ_o . For the reference model $A_o=1$, so that Equation 9 defines the **reference model** density, ρ_r .

$$\rho_r(h, \phi, \lambda) = \rho_o(h, \phi) \left[1 + \sum_{n=1}^3 A_n \sin(n(\lambda - \lambda_n)) \right] \quad (9)$$

The wave amplitudes and phases must be selected so that the model plus sigmas never produces a negative density. For both the reference and MC models the wave amplitudes and phases are functions of latitude but are not random. It is known that both quantities vary with time and altitude, but such variations are difficult to quantify with the limited MGS data set. Additional variability might be included in the model by introducing random wave amplitudes or phases. For simulating only density variations throughout a mission, such variations are of dubious value since they may be small compared to the variability in A_o to be derived later. However, if a procedure to predict future densities, based on a wave model, is included in the simulation process, introducing random wave phases and amplitudes might provide a more realistic simulation.

It is proposed that the MC process consider A_o as the only random variable in the model. In Equation 8, A_o would be considered a Gaussian random variable with mean equal to unity

and variance to be determined from the MGS data. In this model the wave amplitudes are a fixed fraction of ρ_0 .

4.2.2 Reference Monte Carlo Wave Model

Amplitudes and phases for waves 1, 2 and 3 are shown in Figures 17, 18, and 19, respectively. Model coefficients, A_n and λ_n ($n=1,2,3$) were determined by performing a 30-orbit sliding, least squares solution for six wave parameters and a mean density. Input data are taken from the MGS archive and consist of density and H_s at periapsis. Since data from a few orbits are missing, the 30 orbits may not be contiguous. Further, the time span for 30 orbits is significantly longer at the beginning of the mission than at the end. Consequently, short time scale variations in wave characteristics are averaged more during the earlier phases of MGS. Amplitude is given as a percent of the mean density over the 30-orbit data set.

Parameterized solutions are associated with the mean latitude of periapsis of the 30 MGS orbits and are mapped to the lowest altitude in the 30-orbit set. Hence the model can be thought of as being evaluated along a surface of constant dynamic pressure rather than altitude. Calculations for the equipotential surface and its relationship to the reference ellipsoid can be found in Appendix C. The average periapsis dynamic pressure for MGS was 0.17 N/m^2 with 1σ deviation of 50%. The model is representative of the atmosphere about one scale height above the aerobraking altitude for M-01. Adjusting wave properties for this altitude difference has not been attempted, but if the waves are propagating vertically, smaller amplitudes would be expected at lower altitudes. MG2K has a characteristic height, which can be used to model the decay of wave amplitudes below 100 km. There have also been some indications that the wave structure exists to 160 km [10], but these were limited studies. Without additional data, the simplest recommendation is to assume that both A_n and λ_n are altitude independent.

Straight-line models are utilized so as not to over interpret the results. Since each point represents a 30-orbit data arc, the points are not independent and care must be exercised in interpreting trends. As might be expected, when the amplitude is small, the phase becomes difficult to determine, but is unimportant in this case for MC simulations. In the latitude range of interest for M-01 (40° to 90° N), the results from 40° to 60° N are simply extended to the pole, with some consideration given to the south pole results. The validity of the extrapolation to the pole could have a major impact on the reliability of the MC analysis.

Wave 1 (Figure 20) does not show significant differences between Phase 1 and Phase 2 results in the north polar region. This wave has similar amplitude variations between 0% and 20% at both northern and southern high latitudes. In the mid-latitudes the amplitude suggest some cell structure and somewhat larger average amplitude. Since M-01 is not expected to aerobreak in mid-latitudes, a constant 10% amplitude is selected for wave 1. It is recognized that to maintain density continuity at the poles it is necessary to have zero wave amplitude. It is not included in the wave model because MG2K tapers the wave amplitudes to zero at the poles. The dashed line in Figure 20 defines the proposed wave 1 reference model.

Time of day, expressed as LST, is another variable that can strongly influence density, so night side orbits during Phase 2 are identified in each plot.

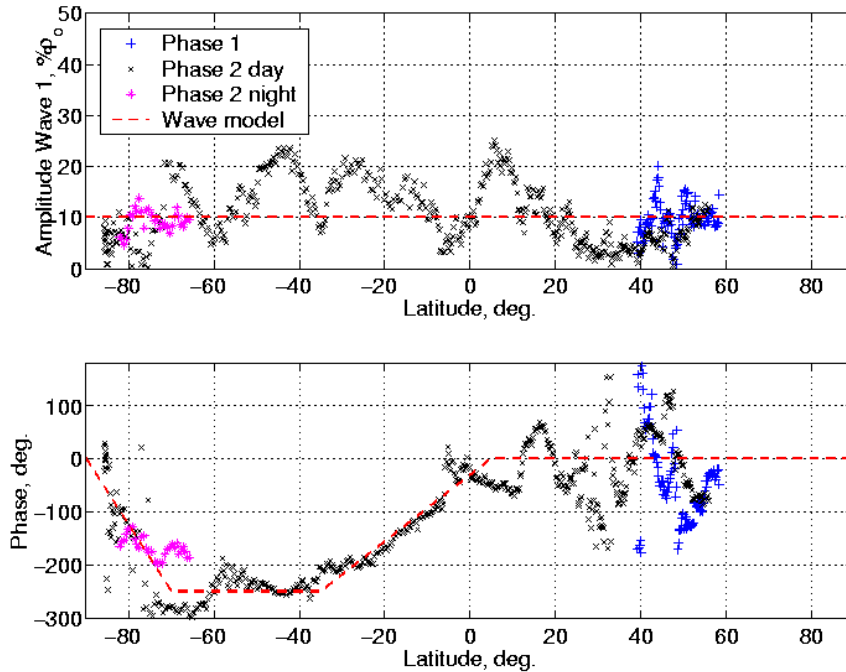


Figure 17. Wave 1 amplitude and phase.

Wave 2 (Figure 18) has a large amplitude in the equatorial region. This has been identified with Kelvin waves [26]. In the region of current interest for M-01, wave 2 phase in the northern hemisphere is about 50 degrees, agreeing with the MGS observation that maximum densities occurred near 100° E longitude. A significant difference is seen between Phase 1 and Phase 2 high northern latitude amplitudes. Latitudes between 38° and 50° (orbits 50-130) correspond to the Noachis storm. Even after the storm appears to have subsided (latitudes 50° to 62°, orbits 130 to 200), the amplitude is still around 20%. The south pole amplitudes, also during winter, are much lower (~10%). One could argue that the large amplitudes during all of Phase 1 are due to the storm and that without stormy conditions the amplitude would be between 5% and 10%. On the other hand, one could argue that the early large amplitudes are due to the storm and the later large amplitudes are due to the northern hemisphere long wave length topography and the resulting atmospheric wave forcing. In the latter case, high north latitude winter conditions will have wave 2 amplitudes of about 20%.

Since M-01 will spend most of the aerobraking phase in this northern latitude range, interpolation can have a large impact. The dashed line defines the proposed reference model when the atmosphere is quiescent and the dot-dashed line represents a turbulent atmosphere. These are respectively called the “low wave” and the “high wave” models. If simulations show that aerobraking can be successfully performed with the “high wave” model, then to be conservative, the “high wave” is the preferred option.

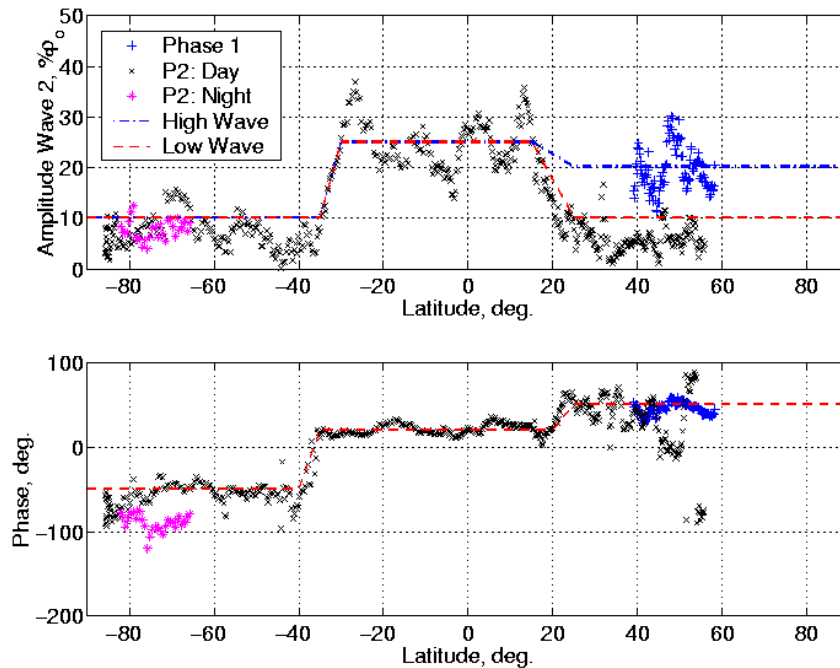


Figure 18. Wave 2 amplitude and phase.

Wave 3 (Figure 19) amplitude data suggest a strong latitudinal gradient in the mid-latitudes (-20° to 60°). This could however be a seasonal change since L_s (Figure 4c) varies from late fall to winter during this time, or this could be due to increased topographic forcing as periapsis passes over the Tharsis latitude range. Nevertheless, M-01 is not expected to aerobrake in this latitude range. There is a lot of variability at the high northern latitudes for both Phase 1 and Phase 2. Both MGS Phases show amplitude increasing toward the pole. Some of this variation may be due to model truncation. It is known that waves up to wave 5 occur in the thermosphere [10]. The wave 3 terms may be absorbing the signal from these

waves. To determine the amount of signal being absorbed by wave 3, an analysis was performed that included the variability from higher order waves 4 and 5. The results are found in Appendix D and show that waves 1 through 3 are sufficient to capture the systematic variations in the Mars atmosphere. The reference model amplitude above 60° N is based on the average amplitude during Phase 1.

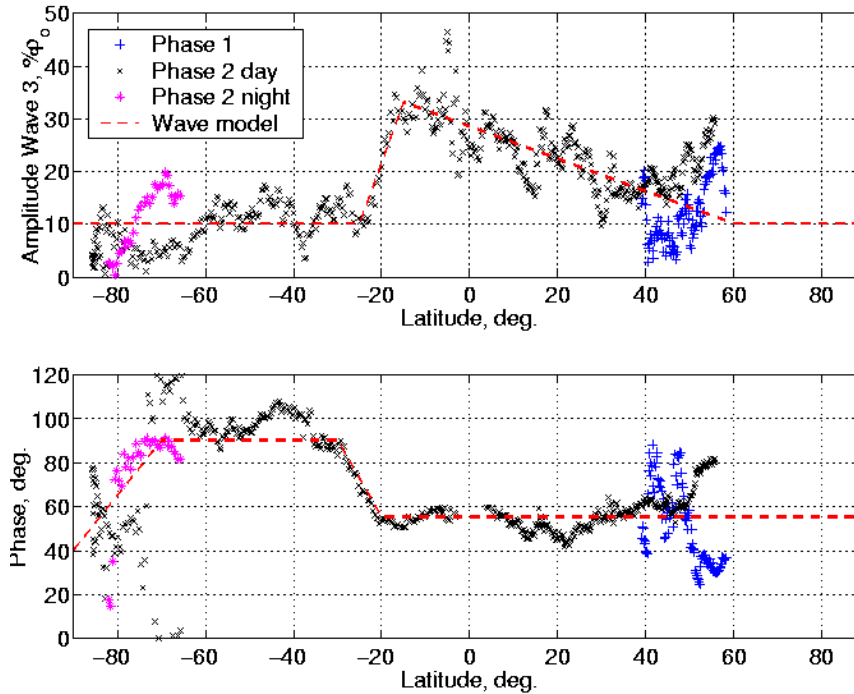


Figure 19. Wave 3 amplitude and phase.

4.3 Monte Carlo Model

Equation 8, which forms the basis of the wave model for MC simulations, requires development of the statistics for A_o . A_o will vary from orbit to orbit and represents the relative difference between the actual density and the wave model predicted density. Each 30-orbit fit to the MGS data provides 30 such residuals or differences between the observed density and the model fit to the observations. For each 30-orbit fit, the mean residual and standard deviation of the residuals can be calculated. The standard deviations are plotted in Figure 20. The mean values are approximately zero. There does appear to be a latitudinal influence in the

standard deviation of the residuals for Phase 2. The values poleward of 40 degrees average around 15% and in the equatorial region average slightly higher at 19%. This equatorial region is the region with the most wave activity and the greater deviation might be due to the fact that the truncated wave model is not capable of absorbing all of the wave effects. To account for this in MC simulations, which are limited to wave 3 for MG2K input purposes, the latitude dependent standard deviation indicated by the dashed line is suggested for the “low wave” model. The dot-dashed line (22%, Figure 20) represents the suggested standard deviation in A_o for the “high wave” model. This increased random variation in A_o along with the increased wave amplitude shown in Figure 18 will provide the most difficult test for any maneuver strategy.

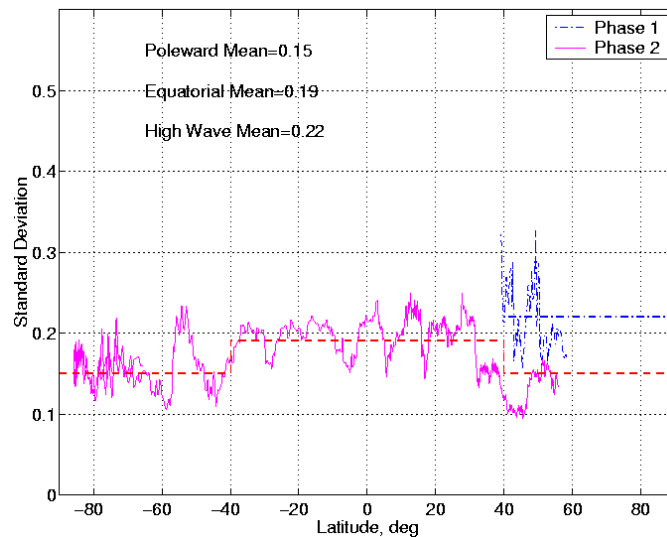


Figure 20. Standard deviation of the residuals for wave model solution.

The analysis has so far provided the mean and standard deviation, so the remaining issue is the distribution function. One approach would be to evaluate the distribution of each 30-orbit fit. This only provides thirty residuals, which is insufficient to provide much confidence in the distribution. On the other hand, most of the MGS orbits were included in 30 different least squares solutions. These appeared as the first orbit, second orbit, up to the

thirtieth. Hence thirty histograms can be made, one for each location in the 30-orbit solution and each with 680 residuals from the 680 MGS orbits. Four of these are shown in Figure 21. The mean values are essentially zero and the standard deviations are within the ranges given in Figure 20. The distribution for these points, as well as the other 26, is nearly normal. Hence the random distribution for A_o in Equation 8 is a 3σ truncated, normal distribution with mean zero and the latitude dependent standard deviation given in Figure 23. However it is recommended that no density less than $0.2\rho_o$ be used.

For the recommended values of the amplitude and phase, the minimum global value for the sum of the three waves is -0.67 and the maximum is 0.58 for both models. Therefore, the waves alone produce a total variation from 33% to 158% of the ρ_o value in Equation 8. The corresponding numbers for latitudes north of 45° N are 81% to 134% for the “low wave” case and 71% to 144% for the “high wave” case. A contour and three-dimensional plot of the “low wave” case is found in Appendix E. When combined with a random variation of Figure 20, it is clear that a negative density can result in the global case but not for latitudes above 45° N.

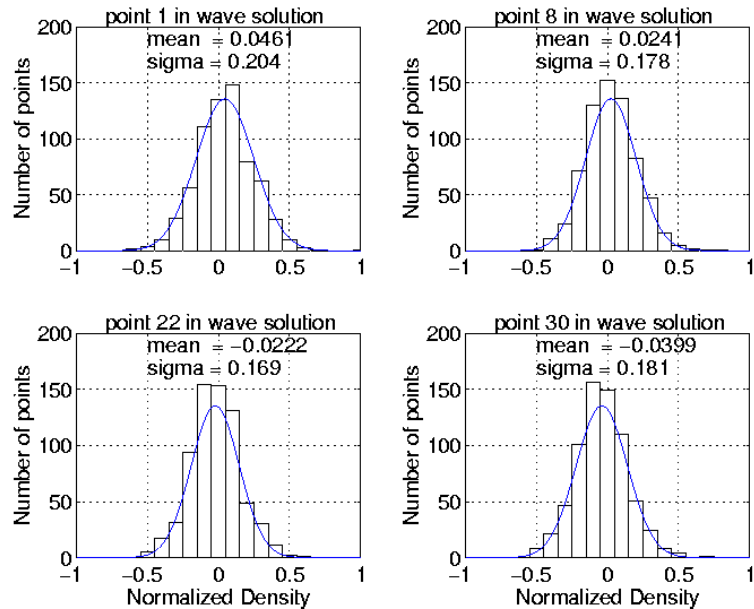


Figure 21. Histograms for points 1, 8, 22, and 30 from sliding wave model solutions.

It should be mentioned that the data used to develop the models include prediction errors as well as atmospheric variability. That is, the periapsis density and H_s are determined from the MGS accelerometer data and have parameter estimation errors. Periapsis density, in most cases, is accurate to a few percent, but H_s estimates are very sensitive to local waves and can introduce large errors in the predicted density if the density is mapped over a large altitude difference. This error source is ignored in this analysis, but should introduce a small degree of conservatism in the models. It is also worthwhile to note that M-01 will perform most of the aerobraking in a latitude range for which there is no MGS data, i.e., above 60° N, and that the MC models are based on extrapolation.

4.4 Model Validation

Three methods will be used to test the validity of the models. Orbit-to-orbit variability has always been a measure of the variation in the Martian atmosphere, so model predicted persistence will be compared to the MGS persistence. The second method will be to determine to what extent the model will reproduce the wave and phase variations shown in Figures 17, 18, and 19. The third method will compare the prediction capability of the model with the MGS data when a 30-orbit wave model is used for prediction.

4.4.1 Persistence Test

Figure 22 provides the persistence results from the MGS archived data set. The plotted ratio is density for orbit $n+1$ as predicted by using orbit n density and H_s over the observed density at orbit $n+1$ or given by the equation

$$\rho_{n+1} = \rho_n e^{-\left(\frac{h_{n+1}-h_n}{H_{s_n}}\right)} \quad (10)$$

In the histogram of Figure 22, a and b are coefficients in the equation for the gamma PDF where the mean of the data is equal to a times b and b is the variance.

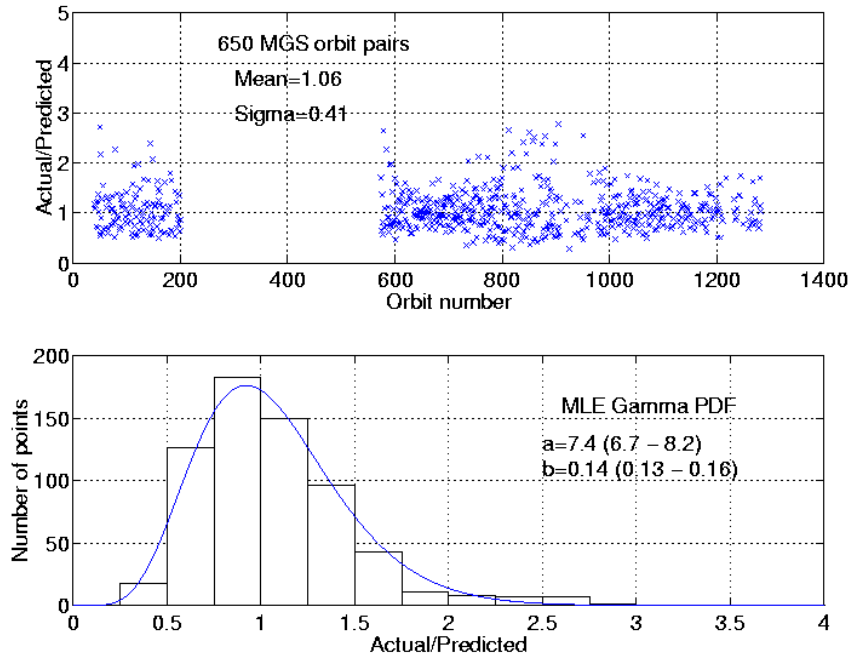


Figure 22. Persistence results using MGS periapsis density and scale height.

Three ratios greater than 5 were deleted from the statistical results. Such unusually large ratios significantly bias the variance and are usually due to local atmospheric phenomena rather than global scale atmospheric variability. During MGS operations, such anomalistic orbits could be identified because the accelerometer (density) data had an unusual variation with time and altitude. These anomalistic results were generally attributed to small-scale waves in the atmosphere and ignored when deciding on maneuver strategy. The maximum likelihood estimates (MLE) of a gamma distribution fit to these ratios are presented in the figure. The 95% confidence limits are presented in the parentheses. The standard deviation of the MLE solution ($\sqrt{0.14} = 0.37$) is only slightly smaller than the standard deviation of the sample (0.41).

To determine how well the MC model reproduces these ratios, densities are simulated by evaluating the models at MGS periapsis latitudes and longitudes and setting $\rho_o=1$ in Equation 8. The persistence ratio is the ratio of adjacent densities. Figure 23 provides one realization of model persistence to be compared to Figure 22.

In Figure 23, the mean (a times b) and the variance (b) are very close to the MGS data. No outliers, i.e., points above a ratio of 5 or below 0.2, were obtained from this simulation. Table 2 provides the statistics for 10 runs of both the “low wave” and “high wave” models. The “low wave” statistics are very consistent from simulation to simulation and agree well with the MGS statistics. The “high wave” sigmas are slightly larger than the MGS value and not as consistent from simulation to simulation. The increase in sigma above the MGS value is partly due to the larger wave 2 amplitudes being applied to the Phase 2 orbits at high northern latitudes. Some simulations from both models provide a few outliers. These occur when a statistically large (small) value for A_o is generated at a longitude that has a large (small) wave contribution. It is possible that this may occur during the mission so no further tuning of the model is required due to these few points.

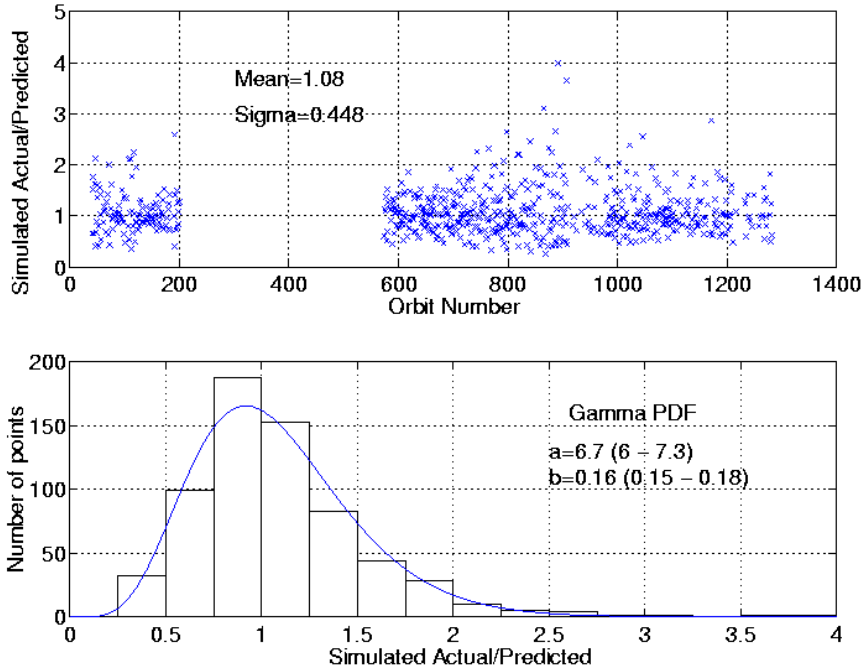


Figure 23. Persistence for one realization of MC model densities.

Table 2. Summary of 10 Realizations of the Monte Carlo Model.

Case	Low Wave			High Wave		
	Mean	Sigma	Outliers	Mean	Sigma	Outliers
1	1.062	0.401	0	1.108	0.750	2
2	1.086	0.481	0	1.076	0.441	0
3	1.073	0.441	0	1.092	0.504	2
4	1.073	0.447	1	1.082	0.462	1
5	1.063	0.400	0	1.093	0.507	4
6	1.069	0.426	0	1.090	0.511	3
7	1.069	0.458	2	1.075	0.436	0
8	1.079	0.462	0	1.076	0.444	0
9	1.079	0.441	0	1.096	0.745	2
10	1.072	0.401	0	1.086	0.498	2
Mean	1.067	0.438	0.3	1.087	0.53	1.6
MGS	1.06	0.41	0	1.06	0.41	0

4.4.2 Reconstruction of Wave Amplitude and Phase

The second test addresses the ability of the model to reconstruct the general nature of the amplitude and phase variations of the waves in the Mars atmosphere. For this test, one

realization of the MGS mission is produced again assuming $\rho_0=1$ and the “low wave” model. Thirty-orbit sliding least squares wave solutions are performed over the entire set of data. Wave amplitudes and phases can then be compared with the actual data values. The question is whether the random component in A_0 will produce realistic deviations in wave amplitudes and phases.

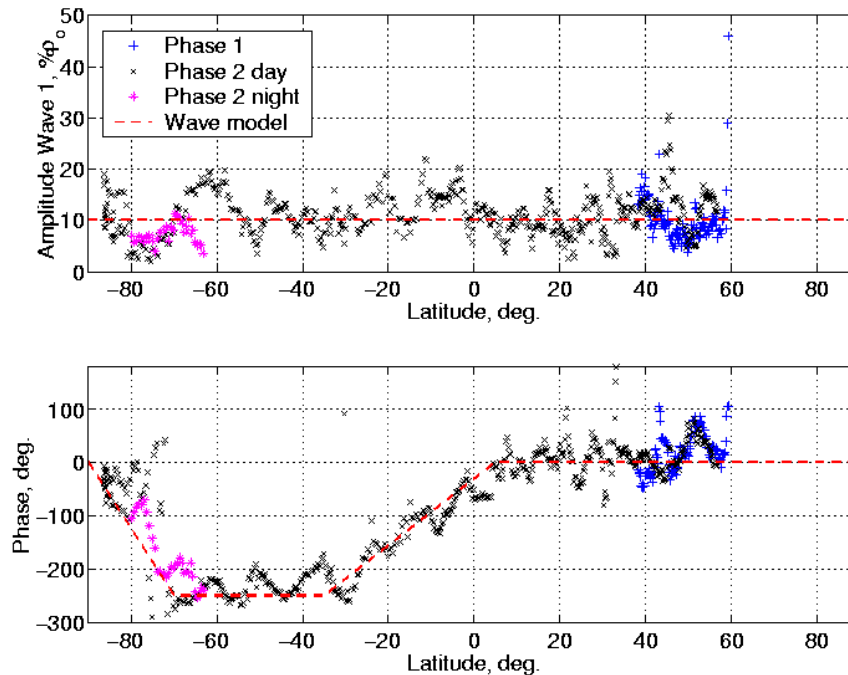


Figure 24. Wave 1 amplitude and phase recovered from one realization of the MC model.

Figure 24 shows the wave 1 amplitude and phase recovered from the MC low wave model generated data. There is very good comparison with Figure 17 in terms of the structure of the deviation of the amplitude and phase from the model values (dashed lines). Likewise Figure 25 shows the wave 2 amplitude and phase recovered from the MC model generated data. There is again very good comparison with Figure 18 in terms of the structure of the deviation of the amplitude and phase from the model values (dashed lines). The Phase 1 orbits (blue +) are not in such good agreement because the data are from the “low wave” model. Finally, Figure 26 shows the wave 3 amplitude and phase recovered from the MC model generated data.

There is very good comparison with Figure 19 in terms of the structure of the deviation of the amplitude and phase from the model values (dashed lines). Though not shown here, similar studies with the “high wave” model provide very good comparisons with Phase 1, wave 2 amplitude.

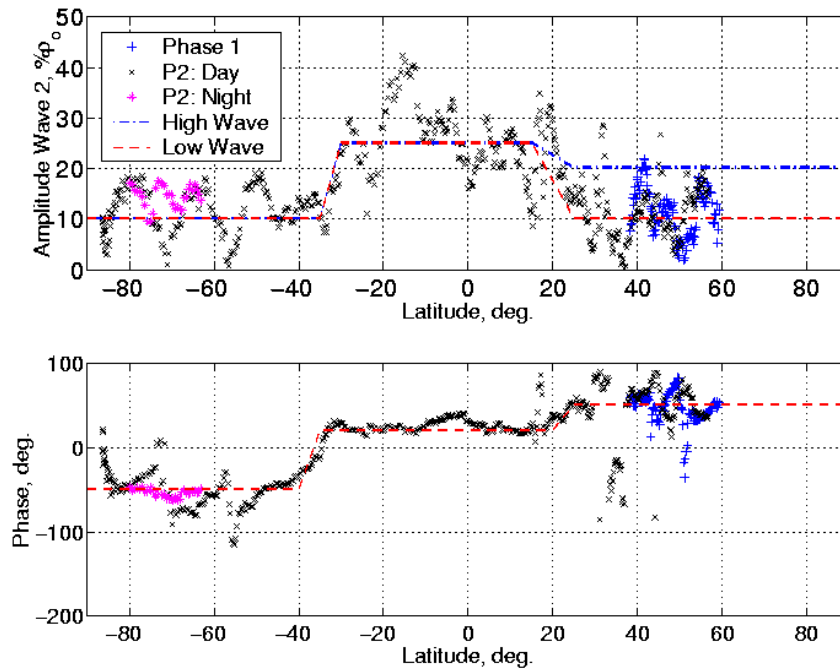


Figure 25. Wave 2 amplitude and phase recovered from one realization of the MC model.

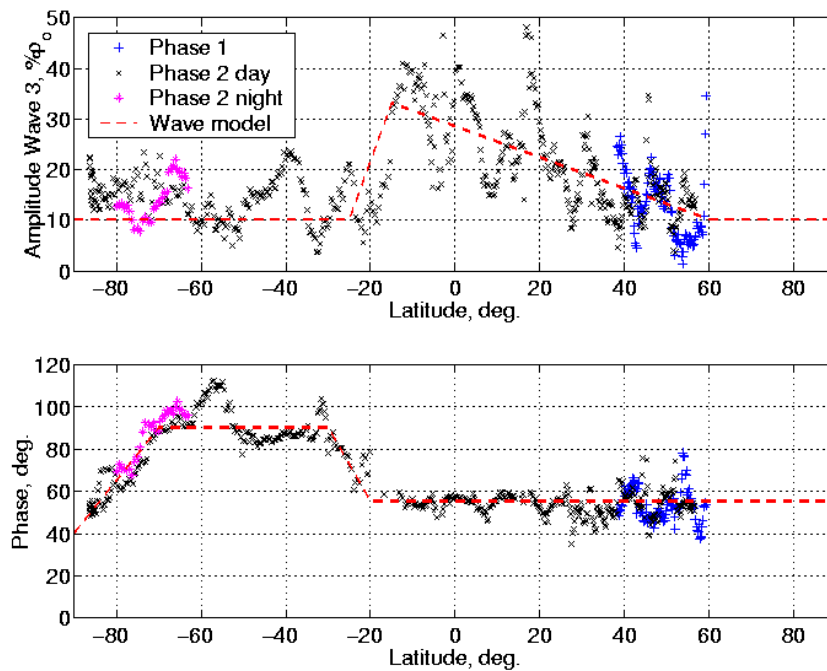


Figure 26. Wave 3 amplitude and phase recovered from one realization of the MC model.

4.4.3 Wave Model Prediction

The final test compares the sliding 30-orbit wave model prediction capability for the MC model and the MGS data. The comparison is limited to Phase 2 data using only the “low wave” model because the model is uniformly consistent with the data, that is, there is no “high wave” data during Phase 2. Figure 27 shows the ability of the 30-orbit sliding wave model solution to predict the density one orbit past the thirty orbits in the solution. The standard deviation of the wave model prediction is typical of MGS operational experience, that is, about 25%- 1σ . This is of course much smaller than orbit-to-orbit persistence shown in Figure 22. The gamma distribution parameters have relatively similar 95% confidence limits, but the variances are consistent.

Figure 28 shows similar results from one realization of the MC “low wave” model for Phase 2. The comparison of statistical metrics is excellent. The MGS data is clearly not homogeneous across the latitude range, where of course the simulated is nearly homogeneous except for the small change in the standard deviation in A_o that occurs at 40° N latitude (see Figure 20). This comparison suggests that maneuver strategies utilizing a sliding wave model solution to predict future density can be performed realistically without requiring random variations in wave amplitudes and phases.

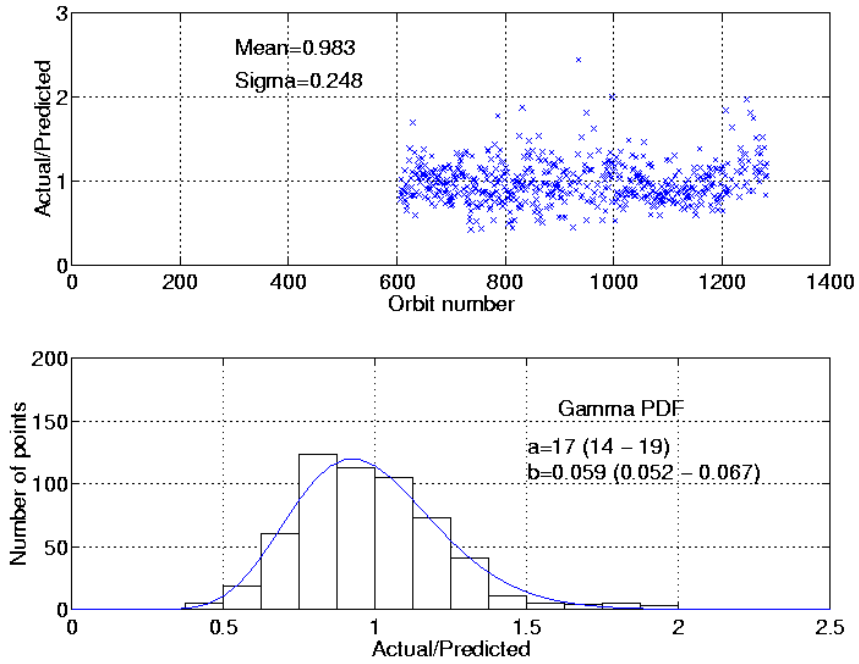


Figure 27. Prediction capability for the 30-orbit wave model solution; MGS Phase 2 data.

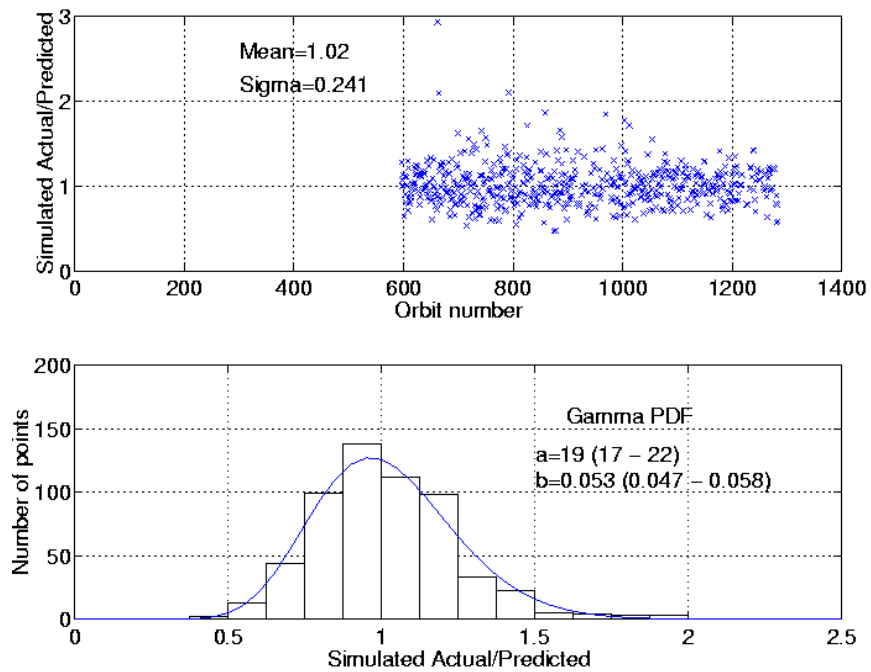


Figure 28. Prediction capability for the 30 orbit wave model solution; MC Phase 2 data.

4.5 Operational Prediction Schemes

During M-01 operations, various schemes will be utilized to estimate future values of density at periapsis. Such schemes might include persistence, running means, wave models, and any new methods that give better predictions. These schemes might be based on Jet Propulsion Laboratory, JPL, Navigation Team density and H_s estimates, accelerometer team density and H_s , and/or MG2K. Maneuver decisions will be based on the results from one or more of these methods. Reviewing Figures 22 and 23 leads to the conclusion that persistence is not a viable scheme and will lead to excessive periapsis “up” and “down” maneuvers.

During MGS operations, trends in the 5-orbit running mean were used, along with trajectory predictions, to make maneuver decisions. The wave model was used to look farther into the future. Orbit-to-orbit decisions were of two types. First there was a “red line” dynamic pressure. If this was exceeded based on accelerometer data, the operations team was authorized to initiate the pre-loaded “up” maneuver. If an unusually high dynamic pressure below the “red line” occurred, the ops team would caucus, compare data and models, and make a decision for subsequent orbits.

MC simulations of aerobraking operations should include some scheme for making both types of decisions as a fundamental part of the process. As an example of expected results from the model, one realization is shown in the upper part of Figure 29. For this example it is assumed that 1.8 is the “spacecraft qualification” limit and the “red line” is set at an arbitrary value of 1.5. In this simulation, 11 points were above 1.5 and two points were above 1.8. For the “low” (“high”) wave model, the 10 simulations shown in Table 2 gave 0.7 (0.8) orbits that exceeded 1.8 and 14.5 (20.9) orbits that exceeded 1.5. To extrapolate to the 200-300 Odyssey aerobraking orbits, divide all counts by 2 or 3. This count is based on “flying at the nominal” when the “red line” events occur. Being high or low in the corridor will change the count. Of

course, in a simulation that includes maneuvers, the entire sequence would be changed after the first maneuver. To evaluate such effects is the rationale for MC simulations.

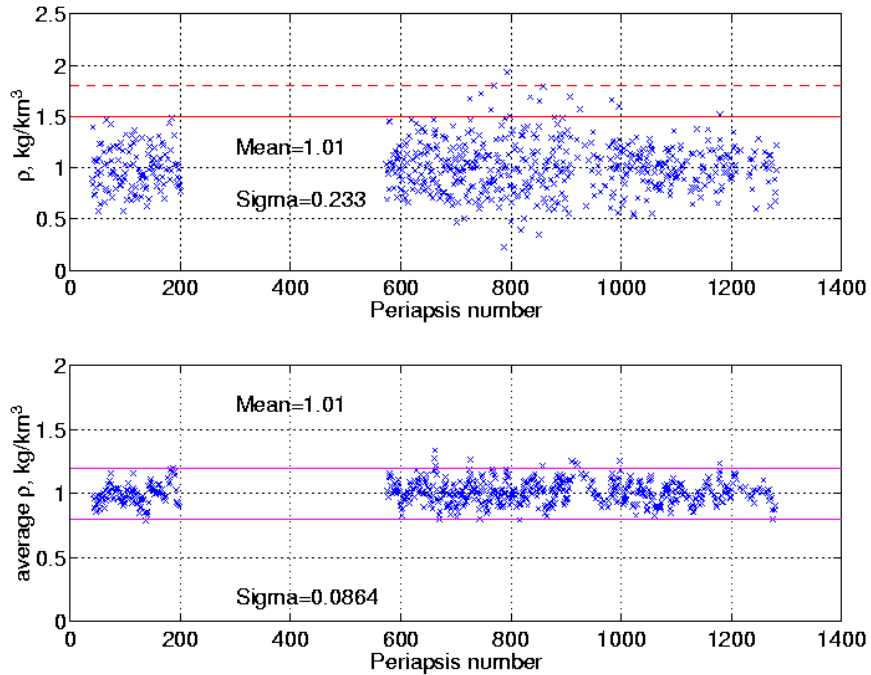


Figure 29. One realization of MC model for MGS: $\rho_0=1$ (ρ) and 5 orbit running mean (ρ_5).

The 5-orbit mean might be used to make maneuver decisions like that shown in the bottom of Figure 29. For example, if two successive 5-orbit means were above the corridor and periapsis was decreasing, then an “up” maneuver would be performed, likewise for “down” maneuvers. If the corridor width is 0.8 to 1.2 (an arbitrary corridor), then the case illustrated in the lower part of Figure 32 has two “up” maneuver and zero “down” maneuvers. These numbers exclude any interaction from prior maneuvers and also assumes the mission is flying the center of the corridor.

4.6 Monte Carlo Model Summary

The “low wave” model that is proposed for the MC simulations is described by the dashed line for amplitudes and phases in Figure 17 through 19 and the dashed line 1σ deviation

given in Figure 20. The decision was made to use the “low wave” model for the phase and amplitude and the “high wave” A_o variation. A_o will be normally distributed about a $15\% \cdot 1\sigma$ from 90° S to 40° S, $19\% \cdot 1\sigma$ from 40° S to 40° N, and $22\% \cdot 1\sigma$ from 40° N to 90° N with each truncated at 3σ . However it is recommended that no density less than 0.2 times the mean density be used.

The implementation of the MC wave model, as suggested in Section 4.1, is currently being done at the NASA Langley Research Center. The MC simulations of the M-01 mission are used to determine the length of the aerobraking and the change in velocity requirements of the mission. Figure 30 depicts a sample M-01 mission obtained by a trajectory simulation using the MC wave model. The figure shows the heat rate indicator as a function of orbit period for one particular simulation of the Mars 2001 aerobraking mission.

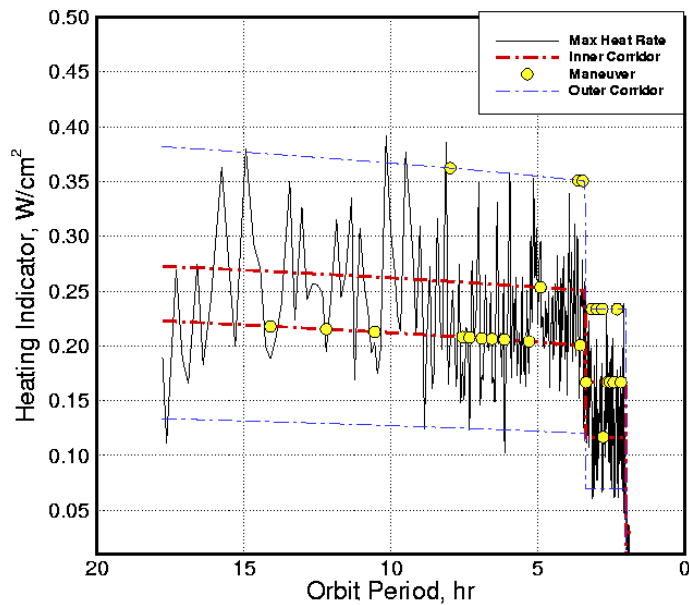


Figure 30. Heat rate versus apoapsis for one Mars 2001 mission simulation.

The density in the atmosphere directly affects the temperature of the spacecraft. Therefore, heating corridors are designed to ensure that the spacecraft does not experience heat rates above the specified qualifications while also ensuring that aerobraking is performed in a

timely manner. This simulation used two heating corridors, similar to the arbitrary “red line” corridor shown in Figure 29. A predictive maneuver strategy was then implemented. The strategy allowed maneuvers to be performed at selected apoapses or slots. From each slot, a prediction of the heat rate for the next n orbits was performed. This defined a prediction span. Therefore, if the heat rate of any orbits in the span exceed the inner corridor more than three times or exceeded the outer corridor more than once, a maneuver would be made to ensure that the heat indicator would remain in the corridor on the subsequent passes. The maximum heating corridor limit is not shown in the figure but is located at approximately 0.58 W/cm^2 for the main aerobraking phase. The limit corresponds to a temperature of 190° C .

The simulated M-01 aerobraking mission, shown in Figure 30, required 379 orbit revolutions over 74.5 days [27]. The mission used fuel associated with an accumulative 19.8 m/s change in velocity required for 31 aerobraking maneuvers used to maintain the spacecraft within the heating corridor.

Finally, the models, proposed herein, are not intended to predict the density of the Martian thermosphere, but rather to provide an approximation to the natural and random variations of the atmosphere. The sole purpose of the development is to provide a statistical model for the M-01 MC simulations of the aerobraking phase.

Chapter 5. Summary

Aerobraking has proved an economical way to explore planets with atmospheres. The success of aerobraking depends on knowledge of the atmosphere, in this case, of Mars. The size, shape of the planet, the evolution of the atmosphere and distance from the Sun establish characteristics of the atmosphere. The lower and upper atmosphere interacts and are affected by diurnal, seasonal, latitudinal, longitudinal variations and the dust present in the atmosphere.

Models are developed that attempt to account for variations and interactions in the atmosphere. One of the widely used models is Mars-GRAM. Versions of Mars-GRAM are continually being upgraded. The Mars-GRAM 2000 version was selected for the M-01 aerobraking operations and simulations because, in comparisons with other Mars-GRAM versions, the density prediction in the winter polar region, where M-01 aerobraking is expected to take place, were closer to the measured MGS value. MG2K also permits wave model inputs. A wave model was developed based on MGS data to be implemented in MG2K. To obtain densities that more closely match those obtained during MGS, an altitude offset was also incorporated into the MG2K version designed specifically for the M-01 mission.

The significant amount of density data obtained from MGS prompted the development of a statistical model of the atmosphere that would enable MC simulations of the M-01 aerobraking operations using both the Odyssey version of MG2K and the wave model. The statistical model introduced a latitudinal dependent, normally distributed, random multiplier on the mean density. For the “low wave” nominal model, the magnitude of the multiplier was 15% poleward of 40° and 19% in the equatorial region with each truncated at $3\text{-}\sigma$. The random multiplier was included to capture the variability in the Mars atmosphere. The M-01 mission is the first in which MC simulations based on a wave model has been used to aid in mission

design. Verification of the wave model will be conducted during the M-01 aerobraking mission scheduled to begin in October 2001.

References

1. Munk, M. M. and Powell, R. W., "Aeroassist Technology Planning for Exploration," *American Astronomical Society*, AAS-00-169.
2. Lyons, D. T., "Aerobraking Magellan: Plan Versus Reality" *Advances in Astronautical Sciences*. AAS 94-118, Vol. 87, Part II, 1994, pp. 663-680.
3. Tolson, R. H. *et al.*, "Applications of Accelerometer Data to Mars Global Surveyor Aerobraking Operations," *Journal of Spacecraft and Rockets*, Vol. 36, No. 3, May-June 1999, pp. 323-329.
4. Part 1: Aerobraking Background and "The Plan" Before the Start of Aerobraking. Online. NASA, JPL. Available: mars.jpl.nasa.gov/mgs/confirm/aerobexp.html.
5. Cooper, D. M. and Arnold, J. O., "Technologies for Aerobraking," NASA TM 102854, March 1991.
6. Bougher, S. W., *et al.*, "Mars Global Surveyor Aerobraking: Atmospheric Trends and Model Interpretation," *Advanced Space Research*, Vol. 23, No 11, 1999: pp. 1887-1897.
7. Kondratyev, K. Y. and Hunt, G. E., *Weather and Climate on Planets*, New York: Pergamon, 1982.
8. Kaplan, D. I., *Environment of Mars*, NASA TM 100470, 1988.
9. Keating, G. M., *et al.*, "The Structure of the Upper Atmosphere of Mars: In-Situ Accelerometer Measurements from Mars Global Surveyor," *Science*, Vol. 279, No. 5357, 1998: pp.1672-1676.
10. Tolson, R. H., *et al.*, "Utilization of Mars Global Surveyor Accelerometer Data for Atmospheric Modeling," *Astrodynamics 1999*, Vol. 103, *Advances in the Astronautical Sciences*, edited by K. C. Howell, *et al.*, American Astronomical Society, AAS-99-386.
11. Mars Pathfinder-Surface Weather Report. Online. NASA Kennedy Space Center. Available: science.ksc.nasa.gov/mirrors/jpl/pathfinder/science/weather.html.
12. Christensen, P.R., *et al.*, "Results from the Mars Global Surveyor Thermal Emission Spectrometer," *Science*, Vol. 279, No. 5357, 1998, pp. 1692-1697.
13. Justus, C.G. and James, B. F. "Mars Global Reference Atmospheric Model 2000 Version (Mars-GRAM 2000): Users Guide," NASA TM-210279, May 2000.
14. Keating, G. M., *et al.*, "Recent Mars Global Surveyor Acceleration Experiment Results: Day/Night Variations and Changes in Planetary Wave Activity in the Southern

- Hemisphere,” Proceedings of the 25th General Assembly of the European Geophysical Society, Nice, France, April 2000.
15. Justus, C. G. and James, B. F., Johnson, D. L., “A Revised Thermosphere for the Mars Global Reference Atmospheric Model (Mars-GRAM Version 3.4),” NASA TM-209629, May 1999.
 16. Justus, C. G., James, B. F. and Johnson, D. L., “Recent and Planned Improvements in the Mars Global Reference Atmospheric Model (Mars-GRAM),” *Advances in Space Research*, Vol. 19, No. 8, 1997, pp. 1223-1231.
 17. Read, P. L. *et al.*, “A GCM Climate Database for Mars: For Mission Planning and for Scientific Studies,” *Advances in Space Research*, Vol. 19, No. 8, 1997, pp. 1213-1222.
 18. Bougher, S. W., Murphy, J. and Haberle, R. M., “Dust Storm Impacts on Mars Upper Atmosphere.” *Advances in Space Research*, Vol. 19, No. 8, 1997, pp. 1255-1260.
 19. Culp, R. D. and Stewart, I., “Time-Dependent Model of the Martian Atmosphere for Use in Orbit Lifetime and Sustenance Studies,” *Journal of the Astronautical Sciences*, Vol. 32, No. 3, July-Sept. 1964, pp. 329-341.
 20. Clancy, R. T., “Global Changes in 0-70 km Thermal Structure of the Mars Atmosphere Derived from 1975 to 1898 Microwave CO Spectra,” *Journal of Geophysical Research*, Vol. 95, No. B9, Aug. 30, 1990, pp. 14,543-14,554.
 21. Justus, C. G. and James, B. F. “Mars Global Reference Atmospheric Model (Mars-GRAM) Version 3.8: Users Guide,” NASA TM-209629, May 1999.
 22. Keating, G. M., Private communication, 2000.
 23. Justus C. G., Private communication, 2000.
 24. Bougher, S. W., Private communication, 2000.
 25. Lyons, D. T., *et al.*, “Mars Global Surveyor: Aerobraking Mission Overview,” *Journal of Spacecraft and Rockets*, Vol. 36, No. 3, 1999, pp. 307-313.
 26. Wilson, R. J. and Hamilton K., "Comprehensive model simulation of thermal tides in the Martian atmosphere," *Journal of Atmospheric Sciences*, Vol. 53, No. 9, 1996, pp. 1290-1326.
 27. Tartabini, P. V., Private Communication, 20 June 2001.
 28. Seidelmann, K., Explanatory Supplement to the Astronomical Almanac, University Science Books, Mill Valley, CA, 1992.

Appendix A. Aerobraking in a Constant Density Scale Height Atmosphere

Consider an atmosphere with a constant density scale height, so that the density at any altitude can be written as

$$\rho(h) = \rho(h_o) \exp\left[\frac{-(h-h_o)}{H_s}\right] \quad (\text{A1})$$

where h_o is the reference altitude and H_s is the density scale height. To produce the familiar “bell” shaped density versus time profile, expand the altitude in a Taylor series about the time of periapsis to get

$$h(t) = h(t_p) + \frac{1}{2} \ddot{h}(t_p)(t-t_p)^2 + O((t-t_p)^4) \quad (\text{A2})$$

where $\ddot{h}(t_p)$ is the second derivative of altitude with respect to time evaluated at periapsis.

Assuming a spherical planet, altitude is symmetric in time so odd derivatives vanish and the truncated terms are of order $(t-t_p)^4$ and negligible except during the “walk out.” Picking the reference altitude in Equation A1 to be periapsis and eliminating altitude in favor of time using Equation A2 yields

$$\rho(t) = \rho(t_p) \exp\left[\frac{-\ddot{h}(t_p)(t-t_p)^2}{2h_s}\right]. \quad (\text{A3})$$

This equation demonstrates the “bell” shape variation of density with time.

It is of interest to write \ddot{h} in terms of the orbital elements. Starting with the radial acceleration equation

$$\ddot{r} = r\dot{\theta}^2 - \frac{\mu}{r^2} \quad (\text{A4})$$

where μ is the gravitational constant for the planet and θ is the angular position in orbit. At periapsis $r=r_p=a(1-e)$ and $r^2\dot{\theta}^2 = V_p^2 = \mu(1+e)/r_p$, where V_p is the velocity at periapsis and e is the orbital eccentricity. Since $\ddot{h} = \ddot{r}$ for a spherical planet, Equation A4 reduces to

$$\ddot{h} = \frac{\mu e}{r_p^2}. \quad (\text{A5})$$

To demonstrate the square root of scale height law, first write the standard form for the Gaussian distribution

$$f(x, \mu, \sigma) = \frac{1}{\sigma\sqrt{2\pi}} \exp\left[-\frac{(x-\mu)^2}{2\sigma^2}\right] \quad (\text{A6})$$

where μ is the mean and σ is the standard deviation and

$$\int_{-\infty}^{\infty} f(x) dx = 1. \quad (\text{A7})$$

Comparing Equation A6 and Equation A3 suggests the substitution $\sigma^2 = \frac{H_s}{\dot{h}_p} = \frac{H_s r_p^2}{\mu e}$, leading to Equation A3 in the form

$$\rho(t) = \rho(t_p) \sqrt{\frac{2\pi r_p^2 H_s}{\mu e}} \left[\frac{1}{\sigma\sqrt{2\pi}} \exp\left[\frac{-(t-t_p)^2}{2\sigma^2}\right] \right]. \quad (\text{A8})$$

From Equation A7, the integral over the entire pass is

$$\int_{-\infty}^{\infty} \rho(t) dt = \rho(t_p) \sqrt{\frac{2\pi r_p^2 H_s}{\mu e}} \quad (\text{A9})$$

where $e>0$ is assumed. This result shows that the area under the density curve is proportional to the square root of the scale height and inversely proportional to the square root of the eccentricity. The only approximation to arrive at Equation A9 is the truncation of the Taylor

series in Equation A2 and as long as the scale height is small compared to the apoapsis altitude the higher order terms are not significant.

From a spacecraft viewpoint, the integrals of dynamic pressure ($\frac{1}{2}\rho V^2$) for total drag effect or free stream heat flux ($\frac{1}{2}\rho V^3$) for total heat input are more important variables than density. However, under the same assumptions for which Equation A9 is valid, the velocity variation throughout the aerobraking pass varies by only a few percent from the value at periapsis. So, for example, the total heat input during a pass is closely approximated by the value of the heat flux at periapsis times the radical in Equation A9.

Finally, if the “drag duration” (T_d) is defined as the time from the inbound occurrence of 1% of maximum density to the outbound time when the density is 1% of maximum density, then the drag duration is twice the time for the spacecraft to increase in altitude above periapsis by $4.6H_s$. From Equation A2 and Equation A5

$$T_d = 2\sqrt{\frac{9.2H_s r_p^2}{\mu e}}. \quad (\text{A10})$$

Appendix B. Namelists for MG3.7 and MG2K

Explanation of NAMELIST variables for Mars-GRAM 3.7 [21]

LSTFL	=	List file name (CON for console listing)
OUTFL	=	Output file name
MONTH	=	month of year
MDAY	=	day of month
MYEAR	=	year (4-digit; 1970-2069 can be 2-digit)
NPOS	=	max # positions to evaluate (0 = read data from trajectory input file)
IHR	=	GMT hour of day
IMIN	=	minute of hour
SEC	=	second of minute (for initial position)
ALSO	=	starting Ls value (degrees) for dust storm (0 = none)
INTENS	=	dust storm intensity (0.0 - 3.0)
RADMAX	=	max. radius (km) of dust storm (0 or >10000 = global)
DUSTLAT	=	latitude (degrees) for center of dust storm
DUSTLON	=	West longitude (deg) for center of dust storm
F107	=	10.7 cm solar flux (10^{*-22} W/cm ^{**2} at 1 AU)
STDL	=	std. dev. for thermosphere variation (-3.0 to +3.0)
MODPERT	=	perturbation model; 1=random, 2=wave, 3=both
NR1	=	starting random number (0 < NR1 < 30000)
NVARX	=	x-code for plotable output (1=hgt above ref. ellipse)
NVARY	=	y-code for 2-D plotable output (0 for 1-D plots)
LOGSCALE	=	0=regular linear scale, 1=log (density), 2=COSPAR deviations
FLAT	=	Initial latitude (N positive), degrees
FLON	=	initial longitude (West positive), degrees
FHGT	=	initial height (km), above ref. ellipse
DELHGT	=	height increment (km) between steps
DELLAT	=	Latitude increment (deg) between steps
DELLON	=	West longitude increment (deg) between steps
DELTIME	=	time increment (sec) between steps
CF0	=	climate adjustment factor at surface
CF5	=	climate adjustment factor at 5 km
CF10	=	climate adjustment factor at 10 km
CF15	=	climate adjustment factor at 15 km
CF30	=	climate adjustment factor at 30 km
CF50	=	climate adjustment factor at 50 km
CF75	=	climate adjustment factor at 75 km
deltaZF	=	adjustment for height of 1.26 nbar level (ZF, km)
deltaTF	=	adjustment for temperature at height ZF (K)
deltaTEX	=	adjustment for exospheric temperature (K)
CFp	=	climate adjustment factor for surface pressure
Ipopt	=	interpolation option 0=regression, 1=hydrostatic
rpscale	=	scale factor for perturbations (1=nominal)
NMONTE	=	number of Monte Carlo runs to do
iup	=	LIST and graphics file output option (0=none) [.ne. 0 means normal output of files (default)]

Explanation of NAMELIST variables for Mars-GRAM 2000 [13]

LSTFL	=	List file name (CON for console listing)
OUTFL	=	Output file name
TRAJFL	=	(Optional) Trajectory input file. File contains time (sec) relative to start time, height (km),

latitude (deg), longitude (deg W if LonEW=0, deg E if LonEW=1, see below)

WaveFile = (Optional) file for time-dependent wave coefficient data. See file description under parameter iuwave, below.

DATADIR = Directory for COSPAR data and topographic height data

GCMDIR = Directory for GCM binary data files

MONTH = month of year

MDAY = day of month

MYEAR = year (4-digit; 1970-2069 can be 2-digit)

NPOS = max # positions to evaluate (0 = read data from trajectory input file)

IHR = UTC (GMT) hour of day

IMIN = minute of hour

SEC = second of minute (for initial position)

LonEW = 0 for input and output West longitudes positive; 1 for East longitudes positive

Dusttau = Optical depth of background dust level (no time-developing dust storm, just uniformly mixed dust), 0.3 to 3.0, or use 0 for a Viking-like annual variation of background dust

ALSO = starting Ls value (degrees) for dust storm (0 = none)

INTENS = dust storm intensity (0.0 - 3.0). Storm intensity (>0) must be larger than Dusttau.

RADMAX = max. radius (km) of dust storm (0 or >10000 = global)

DUSTLAT = Latitude (degrees) for center of dust storm

DUSTLON = Longitude (degrees) (West positive if LonEW=0, or East positive if LonEW = 1) for center of dust storm

F107 = 10.7 cm solar flux (10^{*-22} W/cm^{**2} at 1 AU)

STDL = std. dev. for thermosphere variation (-3.0 to +3.0)

NR1 = starting random number (0 < NR1 < 30000)

NVARX = x-code for plotable output (1=hgt above ref. ellipse). See file xycodes.txt

NVARY = y-code for 3-D plotable output (0 for 2-D plots)

LOGSCALE = 0=regular linear scale, 1=log-base-10 scale, 2=percentage deviations from COSPAR model

FLAT = Initial latitude (N positive), degrees

FLON = initial longitude (West positive if LowEW = 0 or East positive if LonEW = 1), degrees

FHGT = initial height (km), above ref. ellipse

DELHGT = height increment (km) between steps

DELLAT = Latitude increment (deg) between steps (Northward positive)

DELLON = Longitude increment (deg) between steps (Westward positive if LonEW = 0, Eastward positive if LonEW = 1)

DELTIME = time increment (sec) between steps

deltaTEX = adjustment for exospheric temperature (K)

rpscale = random perturbation scale factor (0-3)

NMONTE = number of Monte Carlo runs

iup = 0 for no LIST and graphics output, or unit number for output

WaveA0 = Mean term of longitude-dependent wave multiplier for density

WaveA1 = Amplitude of wave-1 component of longitude-dependent wave multiplier for density

Wavephi1 = Phase of wave-1 component of longitude-dependent wave multiplier (longitude, with West positive if LonEW = 0, East positive if LonEW = 1)

WaveA2 = Amplitude of wave-2 component of longitude-dependent wave multiplier for density

Wavephi2 = Phase of wave-2 component of longitude-dependent wave multiplier (longitude, with West positive if LonEW = 0, East positive if LonEW = 1)

WaveA3 = Amplitude of wave-3 component of longitude-dependent wave multiplier for density

Wavephi3 = Phase of wave-3 component of longitude-dependent wave multiplier (longitude, with West positive if LonEW = 0, East positive if LonEW = 1)

iuwave = Unit number for (Optional) time-dependent wave coefficient data file "WaveFile" (or 0 for none). WaveFile contains time (sec) relative to start time, and wave model coefficients (WaveA0 thru Wavephi3) from the given time to the next time in the data file.

Wscale = Vertical scale (km) of longitude-dependent wave damping at altitudes below 100 km (10<=Wscale<=10,000 km)

Appendix C. Equipotential Surfaces and the Relationship to Reference Ellipsoid

The external gravity potential of a planet [28] is given by

$$U_g(r, \phi, \lambda) = -\frac{\mu}{r} \left[1 + \sum_{n=1}^{\infty} \left(\frac{R}{r} \right)^n \sum_{m=0}^n (C_{nm} \cos m\lambda + S_{nm} \sin m\lambda) P_{nm}(\sin \phi) \right]. \quad (\text{C1})$$

where λ is longitude, R is the reference radius (arbitrary but usually the mean equatorial radius), ϕ is latitude and P_{nm} is the associated Legendre polynomial of degree n and order m . C_{nm} and S_{nm} are spherical harmonic coefficients, $\cos m\lambda P_{nm}(\sin \phi)$, and $\sin m\lambda P_{nm}(\sin \phi)$ are the surface spherical harmonics and r is the distance from the origin of the coordinate system. Note that $J_n = -C_n$ and if the origin is taken at the center of mass of the body, C_{10} , C_{11} , and S_{11} vanish.

For a fixed point with respect to a rotating planet, an extra term must be added to account for the centrifugal force so that the net potential is

$$U = U_g - \frac{1}{2} \omega^2 r^2 \cos^2 \phi \quad (\text{C2})$$

where ω is the rotational rate of the planet. Ignoring numerous perturbations that can change the surface shape including (a) atmospheric effects like wind shear, (b) spatial variations in barometric pressure, and (c) ocean currents, the surface of a lake or ocean must be equipotential. If the surface was not of equal potential, the gradient of the potential would not be normal to the surface and the liquid would flow to make the surface equipotential. Similarly, if an atmosphere is rotating rigidly with the planet and there are no dynamic effects, constant pressure surfaces must be equipotential or a flow would result.

The first approximation to the shape of the equipotential surface can be obtained from the central gravity term, the J_2 term and the centrifugal potential

$$U = -\frac{\mu}{r} \left[1 - J_2 \left(\frac{a}{r} \right)^2 \left(\frac{3}{2} \sin^2 \phi - \frac{1}{2} \right) \right] - \frac{1}{2} \omega^2 r^2 \cos^2 \phi \quad (C3)$$

Factoring out a $-\mu/r$ term, equation C3 can be written as

$$U = -\frac{\mu}{r} \left[1 - J_2 \left(\frac{a}{r} \right)^2 \left(\frac{3}{2} \sin^2 \phi - \frac{1}{2} \right) + \frac{\omega^2 r^3}{2\mu} \cos^2 \phi \right] \quad (C4)$$

where a is the reference equatorial radius. For the reference ellipsoid shown in Figure C1 define $b=a(1-f)$ as the reference polar radius and f as the flattening of the planet. For the Earth, J_2 is 1.083×10^{-3} and the centrifugal term at the equator is -5.1×10^{-2} , both are small compared to 1. For Mars the J_2 term is 1.959×10^{-3} and the ratio in the centrifugal term contributes -2.28×10^{-3} , also small compared to 1. Therefore these will be considered “small” in the subsequent approximations.

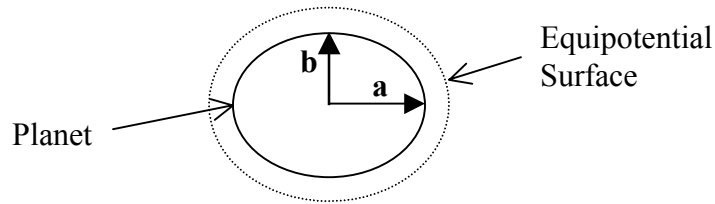


Figure C1. Equipotential surface.

The shape of the equipotential surface tangent to the pole can be found by first setting $r=b$ and $\phi = 90^\circ$ in Equation C4 which yields

$$U_p = -\frac{\mu}{b} \left(1 - J_2 \left(\frac{a}{b} \right)^2 \right). \quad (C5)$$

To determine the radius of this equipotential surface at other latitudes, set Equation C5 equal to Equation C4 and solve for r as a function of latitude. The J_2 term and the centrifugal term are small compared to the μ/r term, so the equations are solved for r from the central gravity term, which gives

$$\frac{1}{r} = \frac{1}{b} + J_2 \left[\left(\frac{a}{r} \right)^2 \left(\frac{1}{r} \right) \left(\frac{3}{2} \sin^2 \phi - \frac{1}{2} \right) - \frac{1}{b} \left(\frac{a}{b} \right)^2 \right] - \frac{1}{2\mu} \omega^2 r^2 \cos^2 \phi. \quad (\text{C6})$$

Using the trigonometric identity $\sin^2 \phi + \cos^2 \phi = 1$ reduces Equation C6 to

$$\frac{1}{r} = \frac{1}{b} + J_2 \left(\frac{a^2}{r^3} \right) - J_2 \left(\frac{a^2}{b^3} \right) - \cos^2 \phi \left(\frac{3}{2} J_2 \left(\frac{a^2}{r^3} \right) + \frac{1}{2\mu} \omega^2 r^2 \right). \quad (\text{C7})$$

For the right hand side, write r as $r = b + \delta r$. Now, assuming $\delta r \ll b$ and using the approximation $(1+x)^p = 1+px$ for small $px \ll 1$,

$$r^{-3} = b^{-3} \left(1 - \frac{3\delta r}{b} \right) \quad \text{and} \quad r^2 = b^2 \left(1 + \frac{2\delta r}{b} \right) \quad (\text{C8})$$

Substituting Equations C8 into Equation C7 yields

$$\frac{1}{r} = \frac{1}{b} \left[1 + J_2 \left(\frac{a^2(b-3\delta r)}{b^3} \right) - J_2 \left(\frac{a^2}{b^2} \right) - \cos^2 \phi \left(\frac{3}{2} J_2 \left(\frac{a^2(b-3\delta r)}{b^3} \right) + \frac{\omega^2 b^2(b+2\delta r)}{2\mu} \right) \right]. \quad (\text{C9})$$

The terms in which the small J_2 and ω are multiplied by the small δr are neglected, so Equation C9 reduces to

$$\frac{1}{r} = \frac{1}{b} \left[1 - \left(\frac{3}{2} J_2 \left(\frac{a}{b} \right)^2 + \frac{\omega^2 b^3}{2\mu} \right) \cos^2 \phi \right]. \quad (\text{C10})$$

Taking the inverse of Equation C10 yields an approximation to the equipotential surface as a function of latitude.

$$r = \frac{b}{\left(1 - \left(\frac{3}{2} J_2 \left(\frac{a}{b} \right)^2 + \frac{\omega^2 b^3}{2\mu} \right) \cos^2 \phi \right)} \quad (\text{C11})$$

The exact equation for a reference ellipsoid [27] is,

$$r^2 = \frac{b^2}{1 - 2f \cos^2 \phi + f^2 \cos^2 \phi} \quad (\text{C12})$$

Taking square root of both sides of Equation C12 and neglecting terms of order f^2 gives

$$r = \frac{b}{1 - f \cos^2 \phi}. \quad (\text{C13})$$

where the $(1+x)^p = 1 + px$ approximation was made.

Equation C11 and C13 are of the same form so the flattening can be related to the J_2 and centrifugal term

$$\frac{b}{(1 - f^* \cos^2 \phi)} = \frac{b}{\left(1 - \left(\frac{3}{2} J_2 \left(\frac{a}{b}\right)^2 + \frac{\omega^2 b^3}{2\mu}\right) \cos^2 \phi\right)} \quad (\text{C14})$$

and

$$f^* = \left(\frac{3}{2} J_2 \left(\frac{a}{b}\right)^2 + \frac{\omega^2 b^3}{2\mu}\right) \quad (\text{C15})$$

where f^* is the approximated flattening. To obtain an approximation of f for Mars, the parameters, $J_2 = 1.95857 \times 10^{-3}$, $a = 3393.4$ km, $b = a(1-f) = 3375.8$ km, $\mu = 4.282823 \times 10^4$ km³/s², and $\omega = 360^\circ/\text{sol} = 7.09 \times 10^{-5}$ rad/s, used by the JPL Navigation Team during Mars Global Surveyor operations are substituted into Equation C15. The resulting f^* is 0.0052262.

This is within 0.3% of the value for flattening used by the Navigation Team of $f = 0.0052083$. Hence the reference ellipsoid has essentially the same flattening as an equipotential surface that considers only the central gravity, centrifugal and J_2 terms. The remaining terms in U_g represent the full equipotential surface and provide variations from the Mars reference ellipsoid of up to 1.2 km.

The difference in kilometers between the reference ellipsoid from Equation C12 and the equipotential surface defined by Equation C7, using $f = 0.0052262$, are seen in Figure C2.

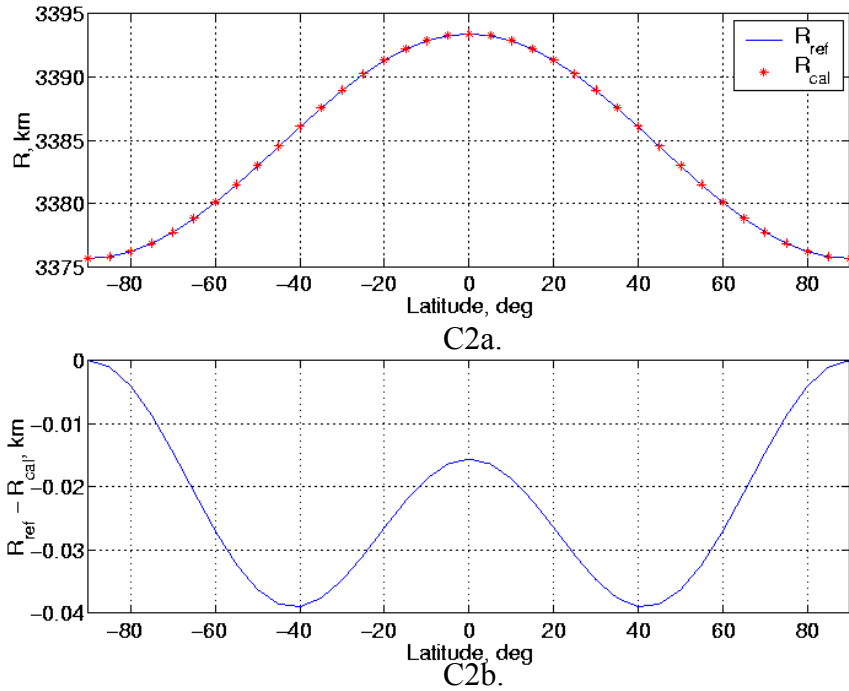


Figure C2a shows the radius of both the reference and approximated ellipsoids, which appear as the same line. Figure C2b shows the difference between the two radii.

The difference in radii results because the f used by the JPL Navigation Team includes the J_4 , J_6 and other even zonal harmonics. However, the reference ellipsoid can be made to agree with the equipotential surface defined only by the central gravity, J_2 and centrifugal terms to within ± 20 meters.

Appendix D. MGS Waves 1 Through 5

The question arose about whether waves 1 through 3 were adequate to describe the variability in the Mars atmosphere. The purpose for this analysis is to determine the amount of variability that results from the higher order waves. The wave analysis was performed using waves 1 through 5 and again solved for using a 30-orbit least squares solution.

Figure D1 shows the results of the least squares solution for wave 1. This plot is to be compared to Figure 19 in Section 4.2.2. The amplitudes and phases look very similar except for the additional scatter in the mid latitudes. The higher amplitudes near 30° , 15° , and -5° latitude result from the resonance of four, five and six Mars Global Surveyor (MGS) orbits per sol (24 hours, 37 minutes) respectively, making it difficult to separate the wave contributions. The orbits per sol for the entire MGS mission can be seen in Figure D6a and are included as annotations in Figures D1 through D6.

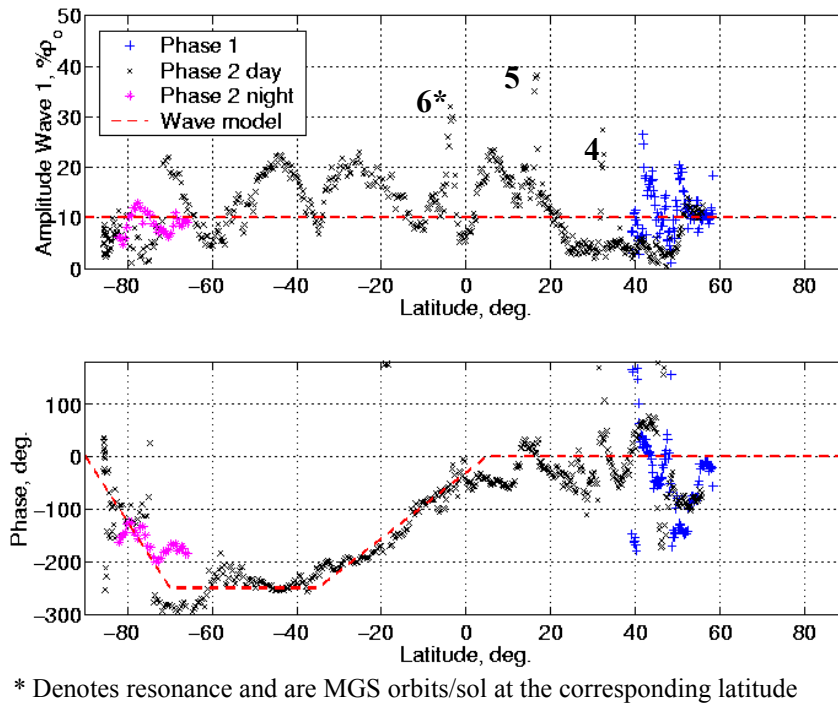


Figure D1. Wave 1 amplitude and phase from 30-orbit least squares solution using MGS periapsis density and scale height. Dashed lines represent the proposed wave model.

The wave 2 analysis in Figure D2 compares well with Figure 20 in Section 4.2.2 with the exception, again, of the mid latitudes. The largest difference occurred while MGS performed 5, 6 and 7 orbits per day. A similar comparison can be made for wave 3 and is shown in Figure D3 and Figure 18.

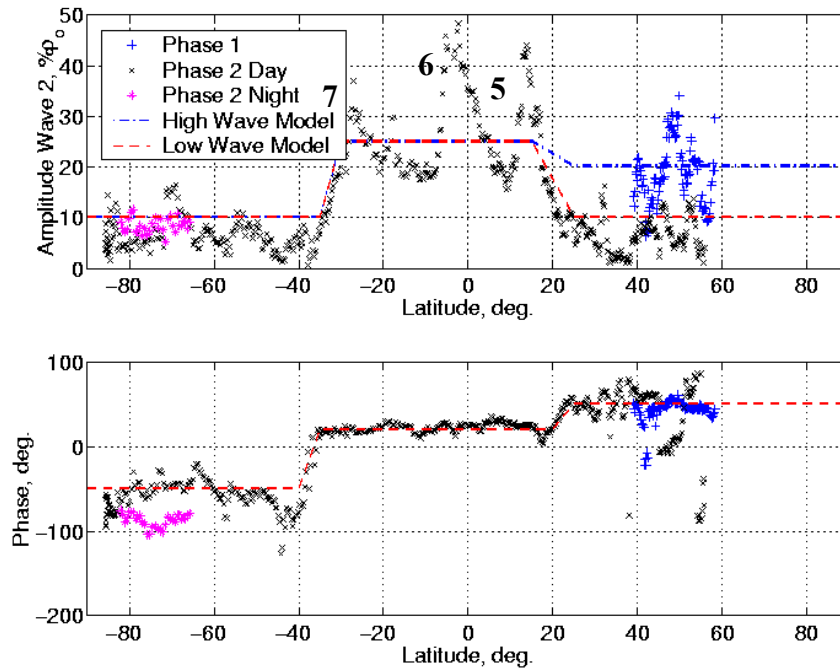


Figure D2. Wave 2 amplitude and phase from 30-orbit least squares solution using MGS periapsis density and scale height. Dashed lines represent the proposed “low wave” model and the dot-dashed lines represent the “high wave” model.

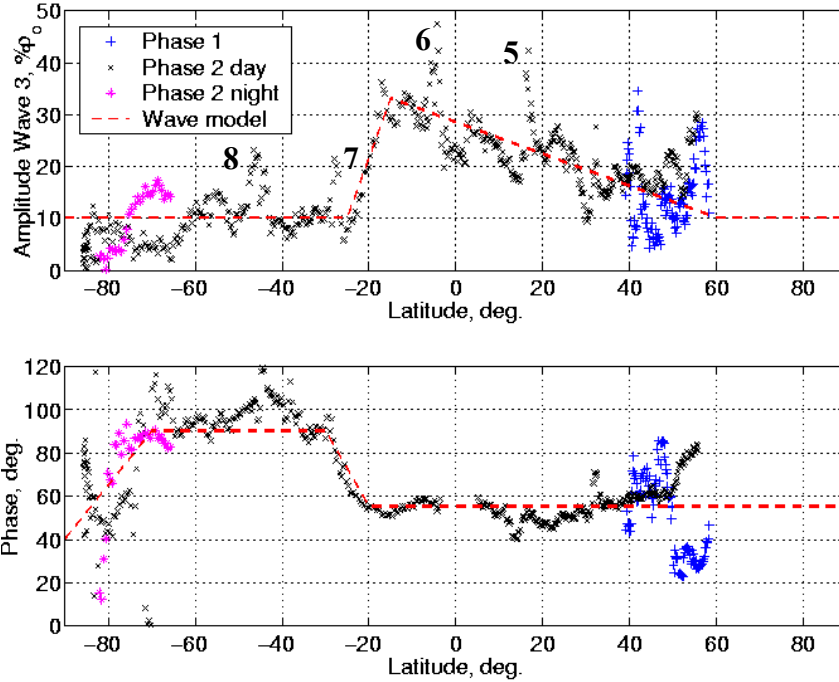


Figure D3. Wave 3 amplitude and phase from 30-orbit least squares solution using MGS periapsis density and scale height. Dashed lines represent the proposed wave model.

Waves 4 and 5 solutions are shown in Figures D4 and D5. Again higher amplitudes are experienced when MGS experienced integer number of orbits in a sol.

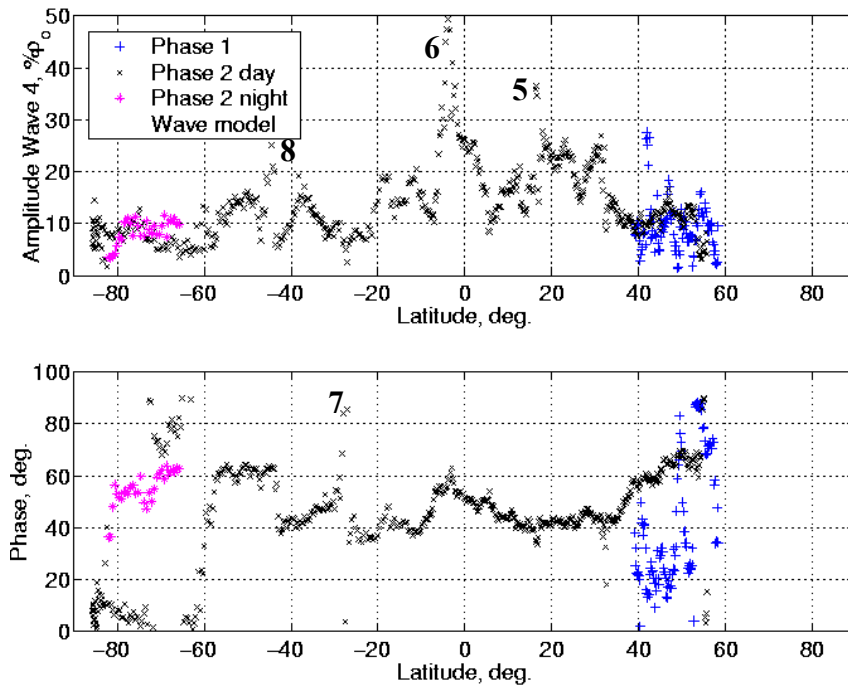


Figure D4. Wave 4 amplitude and phase from 30-orbit least squares solution using MGS periapsis density and scale height.

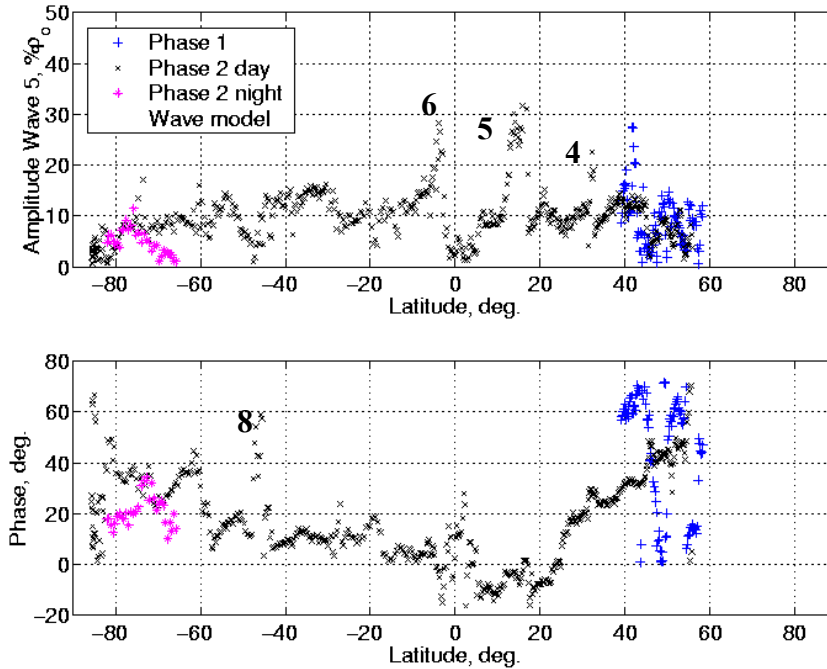


Figure D5. Wave 5 amplitude and phase from 30-orbit least squares solution using MGS periapsis density and scale height.

The correlation matrices between waves 2 and 4 and between waves 3 and 5 were used to generate Figure D6. The eigenvalues of each 4 by 4 correlation matrix were found and the ratio of the minimum to maximum eigenvalue was obtained. Ratios near 1 would represent perfectly uncorrelated estimates of the wave model coefficients. However in the regions where orbital resonance is experienced, the highly correlated results cause very low minimum to maximum eigenvalue ratios (i.e., near 0) suggesting high correlation between estimates and high sensitivity to data noise.

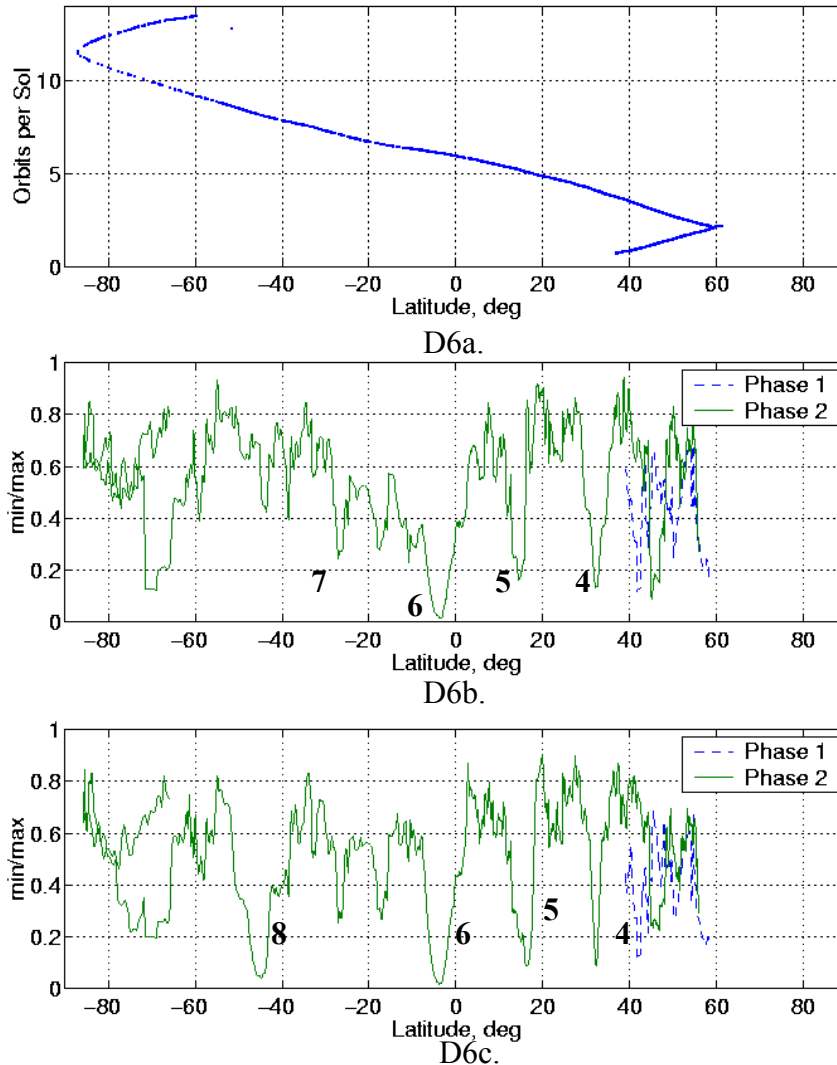


Figure D6 (a) shows the corresponding orbits per sol vs. latitude of MGS data; (b) shows the minimum/maximum eigenvalue ratio from the correlation matrix for waves 2 and 4; (c) shows the same for waves 3 and 5.

Based on the analysis of the MGS data solving for all five waves, waves 1 through 3 look very similar to those presented in the main body of the text. In the region of concern for the M-01 aerobraking the amplitudes of waves 4 and 5 are 10% or less. Also, MG2K is equipped to include waves 1 through 3 only. It is therefore recommended that no change be made to the current proposed reference wave model for purposes of MC analysis. However, the project may want to consider the inclusion of the higher-order waves for predictions during M-01 aerobraking operations.

Appendix E. Plots of the Reference “Low Wave” Model

To provide some physical interpretation of the reference wave model, contour and 3-D plots have been made of the wave model density multipliers. Globally, the contours vary from -0.67 (blue) to 0.58 (red) in 0.05 increments. For latitudes north of 45° N the “low wave” variation is -0.19 to 0.34 . The “high wave,” not pictured, varies from -0.29 to 0.44 north of 45° N.

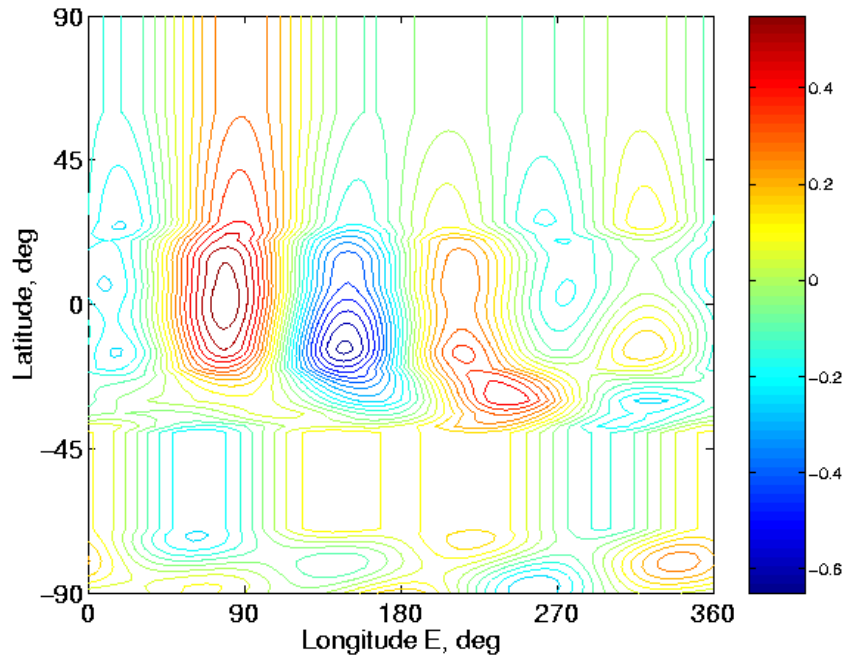


Figure E1. Contour plot of “low wave” density multipliers for a surface of constant pressure over the Mars surface.

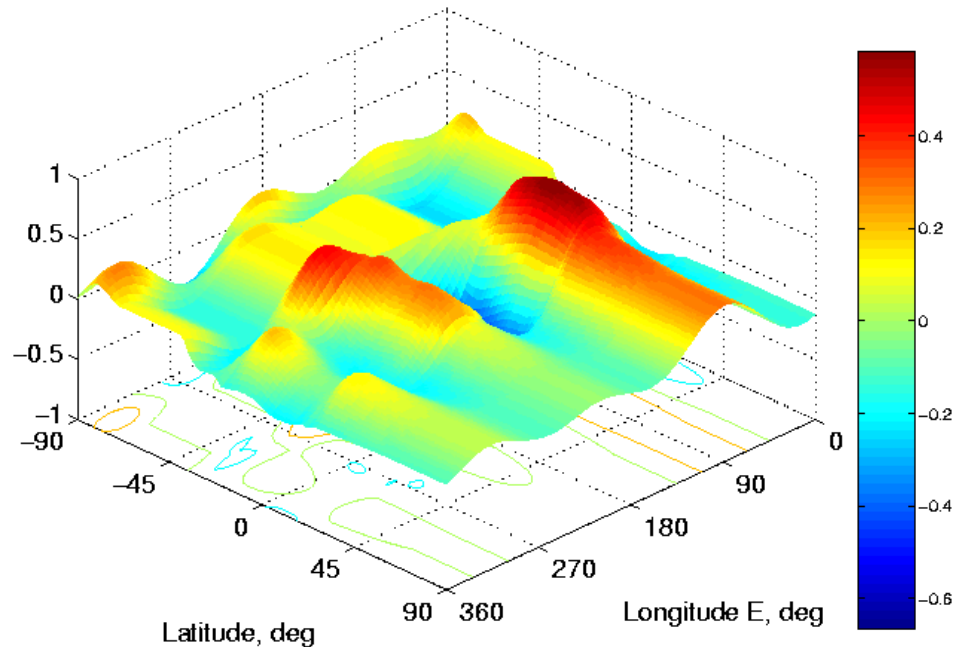


Figure E1. 3-D plot of “low wave” density multipliers for a surface of constant pressure over the Mars.